Sonic Methods and Rock Mass Classification related to Tunnelling in Greenland

Arctic Diploma Project

June 8th - 2009

ARTEK - BYG•DTU

Dan Eggert Møller

s042344

Intentionally left blank

I Nomenclature

Some important symbols and nomenclature occurring in present report and their dimensions, in order of occurrence:

RQD	Rock quality designation [-]
l	Length [m] or [cm] or [mm]
v_p	Compressional wave velocity [km/s] or [m/s]
GSI	Geological strength index [-]
σ_1	Major principal stress [MPa]
σ_3	Minor principal stress [MPa]
σ_c	unconfined (uniaxial) compressive strength [MPa]
σ_t	Tensile strength or indirect tensile strength [MPa]
v_s	Shear wave velocity [km/s] or [m/s]
E	Young's modulus [MPa]
ρ	Density [g/cm^3] or [kg/m^3] or resistivity [Ωm]
K	Bulk modulus [MPa]
M	Modulus of uniaxial strain [MPa]
G	Shear modulus [MPa]
v	Poisson's ratio [-]
K_0	Stress coefficient at rest [-]
λ	Lamé's first parameter [-]
σ	Specific conductance [S/m]
Q	The NGI tunneling index [-]
t	Time [ms] or [μs]
R_N	Schmidt N-type rebound [mm]
R_L	Schmidt L-type rebound [mm]
m	Mass [g] or [kg]
d	Diameter [mm] or [cm]
h	Height [mm] or [cm]

II Preface

Present report is the final product of the academic diploma programme in Arctic Technology at the Arctic Technology Centre (Artek) under BYG•DTU at the Technical University of Denmark (DTU).

The project work and the final report was carried out in the period from February 2nd, 2009, to June 8th , 2009, by engineering student Dan Eggert Møller, student ID. No. s042344, in cooperation with the contracting firm Ístak Ltd. The project has a work load of 20 ECTS points.

Based on a literature study, field investigations and laboratory measurements this report considers geophysical investigations for tunnelling in Greenlandic hard rock and evaluations of rock mass quality based on sonic methods and rock classification in situ.

Supervisors during the project have been Research Professor at BYG•DTU, Lic.Tech. Niels Foged, and Assistant Professor at BYG•DTU, Ph.D. Thomas Ingeman-Nielsen.

Enclosures are placed in a separate document provided with the report.

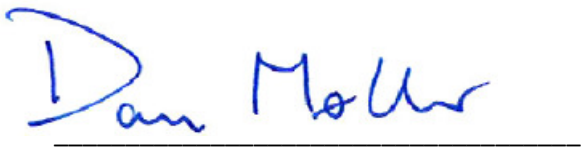

Dan Eggert Møller – 08/06-2009

III Acknowledgements

The author wishes to thank the following people and organisations for their support and cooperation during this project:

Niels Nielsen Foged and Thomas Ingeman-Nielsen for academic supervision.

The Arctic Technology Centre under BYG•DTU for financial aid in relation to accommodation and transport during the field work.

Istak for permission to perform field investigations in the tunnels at the Tasersuaq hydropower project.

Sanaartornermik Ilinniarfik in Sisimiut for usage of laboratory and office facilities.

Larseeraq Skifte at Sisimiut Kommunea for comfortable and exciting transport to and from Istak camp by snowmobile.

IV Extended abstract

Present report presents results from field investigations carried out at the Tasersuaq hydropower project site and laboratory measurements and tests at the Building & Construction School in Sisimiut.

Field investigations were carried out in the parts of the allready excavated tunnel system at the project site. These investigations included refraction seismic surveys, engineering geological mapping and measurements of Schmidt rebounds.

The investigations were conducted along a 90 m profile in what will be referred to as the access/maintenance tunnel, and at a single site at what will be referred to as the pressure tunnel site, which is of interest since a tunnel collapse happened within 25 m of this site. The investigations were restricted to be performed at tunnel segments where the natural ventilation was sufficient to secure good air quality, since the ventilation system was shut down due to the winter hiatus.

Further were samples from the tunnels retrieved to be tested under laboratory conditions, from which reference data were obtained.

To supplement the samples taken from the field sites, already existing cores from the Sisimiut area were selected to undergo the same laboratory testing as the samples from the actual site. The cores were selected to resemble expected rock types from the hydropower site. In all are 6 petrologically different igneous and metamorphic rock types considered in present report, including the sampled rock type from the hydropower project site.

The seismic surveys were originally intended to have been performed as measurement of direct p- and s-wave velocities on the tunnel walls. But this proved to be difficult to realize in practice, since only single-component geophones were available. The alternative was to perform measurements of refracted p-waves, where geophones were inserted into the tunnel floor. This yielded satisfactory results, and the 90 m profile and the single spread were realized.

The engineering geological mapping was performed with the aim of both classifying the rock and discontinuities, and to later calculate the failure envelope of the rock mass. The calculation of the rock mass failure envelope was only possible for the pressure tunnel site, since only from here were the samples large enough to be prepared into specimens which could be tested in unconfined compression as 50mm·50mm·100mm rectangular prisms.

The software RocLab, which is a product available at www.rocscience.com, is used to apply the general Hoek-Brown failure criterion on data from the pressure tunnel site.

The Schmidt hammer rebounds were intended to provide data for evaluating compressive strengths and degree of weathering. Only for the pressure tunnel site was the Schmidt hammer rebounds valid, since the access/maintenance tunnel walls were covered with droplets of shotcrete, which to some degree invalidated the rebound measurements.

Previous investigations, performed during preinvestigations in relation to the hydropower project, will be compared with the findings in present report. The previous investigations include borings, refractions seismic profiling and surface mapping.

The laboratory measurements and tests performed on the samples and supplementary cored specimens includes determination of bulk densities, p-wave velocities, point load indices, unconfined compressive strengths and Brazilian indirect tensile strengths.

Bulk densities are combined with p-wave velocities to form dynamic elastic moduli, with which other obtained parameters of the *intact* rock are compared. Here mainly the correlations with compressive strengths and static moduli are of interest, since these the most relevant in an engineering sense.

The intact p-wave velocities of the from the field sampled rock type, form an upper bound for the in situ p-wave velocities obtained from the refraction seismic surveys. When considering the square of the ratio between intact and in situ p-wave velocities, a measure for the rock quality, specifically the RQD, is obtained.

These calculated rock qualities are then compared with actual tunnel mapping, performed by geologists from Ístak, and is also compared with the tunnel mapping conducted in relation to present report.

The remaining tests, being point load testing and Brazilian tests, form a basis for evaluating the ratios of compressive strength relative to indirect tensile strength, and compressive strength relative to point load index. Further do the unconfined compressive strength and indirect tensile strength form the data basis for calculating the friction angle and internal cohesion, which are determined from envelopes in different stress representations.

The main conclusions from this report are:

There can be obtained a good correlation between velocities in rock obtained from seismic surveys, and actually mapped rock quality descriptors, mainly the rock quality designation RQD. No zones of fatal weakness in the investigated tunnels were identified from refraction seismic velocities, nor from engineering geological mapping.

On a laboratory basis, the dynamic moduli obtained from cored and sampled specimens, and rock properties like unconfined compressive strength and static moduli, follow an increasing trend when correlated values are plotted against each other. The trend cannot be determined satisfactory only utilizing the relatively small data set obtained in relation to this project; the inhomogeneous nature of rock give rise to variance in the obtained data, which require a large data set for a more complete understanding of the trend.

V Udvidet resumé

Nærværende rapport præsenter resultater fra feltundersøgelser udført ved vandkraftprojektet ved Tasersuaq og laboratoriemålinger og –tests ved Bygge- & Anlægsskolen i Sisimiut.

Feltundersøgelserne blev udført i dele af det allerede udgravede tunnelsystem ved byggepladsen. Disse undersøgelser omfattede refraktionsseismik, ingeniørgeologisk kortlægning og målinger af Schmidt-hammer målinger.

Undersøgelser udførtes langs et 90 m langt profil i hvad der vil henvises til som adgangs/vedligeholds-tunnellen, og et enkelt sted, som vil henvises til som tryktunnellen, som er interessant idet et tunnel-kollaps skete nær ved dette sted. Undersøgelser var begrænset til kun at kunne udføres i de dele af tunnelsystemet, i hvilke den naturlige ventilation var tilstrækkelig til at sikre god luftkvalitet, idet ventilationssystemet var ude af drift grundet vinter-pausen.

Endvidere blev prøver fra tunnellerne hjemhentet til undersøgelser i laboratoriet, fra hvilke reference-data blev tilegnet.

Som supplement til prøverne fra felten, blev allerede kerneborede prøveemner fra Sisimiut-området udvalgt til at gennemgå de samme laboratoriemålinger, som de fra felten hjemhentede prøver. Prøveemnerne blev udvalgt på grundlag af sammenlignelighed med de bjergarter, som forventes at findes ved byggepladsen. I alt er 6 petrografisk forskellige vulkanske og metamorfe bjergarter undersøgt i dette projekt, inkluderende prøven hjemtaget fra felten.

De seismiske undersøgelser var oprindelig tiltænkt at være udført som målinger af direkte p- og s-bølger på tunnelvæggene. Men dette viste sig at være for svært gennemførligt i praksis, siden kun enkelt-komponent geofoner var tilgængelige. Alternativet var at udføre målinger på refrakterede p-bølger, hvor geofonerne indsattes på tunnelgulvet. Dette gav tilfredsstillende resultater, og et 90 m langt profil og et enkelt geofon-udlæg blev udført.

Den ingeniørgeologiske kortlægning blev udført ved det i sigte, at både klassificere fjeldet selv og revnersystemer i dette, men også for senere at kunne bestemme fjeldmassens brudbetingelse. Denne bestemmelse var kun mulig for fjeldet ved tryktunnellen, idet kun prøver herfra var støre nok til at kunne tildannes til prøveemner, som kunne testes i enakset tryk som rektangulære, prismatiske prøve-emner med dimensionerne 50mm·50mm·100mm.

Programmet RocLab, som er tilgængeligt på www.rocscience.com, er brugt til anvende den generaliserede Hoek-Brown-brudbetingelse på data fra tryktunnellen.

Det var hensigten, at Schmidt-hammer-målinger skulle bidrage med data til vurdering af trykstyrker og forvitringsgrader. Kun for tryktunnellen var Schmidt-hammer-målingerne gyldige, idet væggene i adgangs-/vedligeholds-tunnellen var dækket med et fint lag sprøjtebeton, som til en vis grad ugyldiggjorde målingerne.

Tidligere undersøgelser, udført under forundersøgelserne til vandkraftværket, vil blive sammenlignet med resultaterne fra denne rapport. De tidligere undersøgelser omfatter boringer, refraktionsseismiske profileringer og geologisk overfladekortlægning.

Laboratoriemålinger og –tests udført på prøver og de supplerende kerneborede prøveemner omfatter bestemmelse af bulk densitet, p-bølgehastigheder, point load indices, enaksede trykstyrker og Brasiliansk indirekte trækstyrke.

Bulk densiteter kombineres med p-bølgehastigheder til at danne dynamiske elastiske moduli, med hvilke, andre parametre for den intakte bjergmasse sammenlignes. De væsentligste korrelationer er dem for enakset trykstyrke og statiske moduli, idet disse er de mest ingeniør-relevante.

De intakte p-bølgehastigheder i bjergarterne hjemhentet fra felten danner en øvre grænse for hastigheder bestemt in situ ved refraktionsseimiske undersøgelser. Når kvadratet på forholdet mellem intakte og in situ hastigheder betragtes, så haves et mål for fjeldkvaliteten, nærmere betegnet RQD-værdien.

Disse beregnede fjeldkvaliteter sammenlignes så med dem fra den faktiske tunnelkortlægning, udført af geologer ved Ístak, og sammenlignes også med tunnelkortlægningen udført i forbindelse med dette projekt.

De resterende tests, værende point load tests og Brasilianske tests, danner et grundlag for bestemmelsen af forholdene mellem enakset trykstyrke og indirekte trækstyrke, og enakset trykstyrke og point load indeks. Endvidere danner de enaksede trykstyrker og de indirekte trækstyrker grundlag for at kunne bestemme friktionsvinkel og indre kohæsion, som bestemmes via brudbetingelser i 4 forskellige spændingsrepræsentationer.

Hovedkonklusioner i denne rapport er:

> Der kan opnås god korrelation mellem hastigheder i hårde bjergmasser beregnet fra refraktionsseismik, og faktisk kortlagte fjeldkvalitetsparametre, primært ”rock quality designation” RQD. Ingen zoner af meget dårlig fjeldkvalitet blev identificeret, hverken ud fra refraktionseismik eller ingeniørgeologisk kortlægning.
>
> Under laboratorieforhold følger dynamiske moduli, bestemt på grundlag af densiteter og p-bølgehastigheder, og bjergartsparametre som den enaksede trykstyrke og statiske moduli, en stigende tendens, når korrelerede værdier opstilles grafisk over for hinanden. Denne tendens kan ikke bestemmes tilfredsstillende med datamængden, som er til rådighed i denne rapport; bjergarters inhomogene natur giver anledning til varians i de fundne data, som fordrer en større datamængde for at kunne beskrive tendensen mere fuldstændigt.

Contents

1 Introduction

In the preinvestigative phase of a civil engineering project which includes construction of tunnels in hard rock, it is of interest to gather as much information possible about the bedrock conditions by means of traditional methods, such as geotechnical borings, engineering geological mapping and seismic surveying.
The obtained information from the different methods can be combined synergistically, to form more nuanced knowledge about the in situ rock mass conditions and parameters. It is the aim of this report to illustrate how this can be achieved. This is done based on a case study of field investigations performed the ongoing hydropower project at Tasersuaq near Sisimiut, Greenland.

To introduce the rock mass quality descriptors used in this project, a very brief presentation of these are given in section 2.1. This section also includes the in present report utilized rock mass failure criterion, called the generalized Hoek-Brown failure criterion. The failure criterion is implemented in the software, courtesy of *Rocscience Inc.*, called *RocLab*, which is used to calculate a rock mass failure envelope for the pressure tunnel site.

Some general notes on the nature of sonic waves is given in section 2.2. This should motivate and supply the reader with some basic concepts of the elastic nature of propagating stress transients, which is a more general term than sonic waves.

To understand how geology affects sonic velocities a brief presentation of influencing parameters is given in section 2.3.

The field investigations included refraction seismic surveying, engineering geological mapping and Schmidt hammer rebound measurements. The methods are presented in section 3.4. The results are presented in sections 5.1 – 5.3, and are discussed in sections 6.1 – 6.3.

Samples of the bedrock in which the tunnels, specifically the access/maintenance and pressure tunnels, were constructed. These were retrieved back to the laboratory, where parameters like bulk density, p-wave velocity, point load index, unconfined compressive strength, Brazilian indirect tensile strength were determined to form a interpretational basis, along with already cored specimen stored at the Building & Construction School. This laboratory work is described in section 4, and the obtained results are presented in sections 5.4 - 5.8 and discussed sections 6.4 - 6.7.

For further reading and background material, the reader is referred to the enclosures 1, 7 and 9.

2 Theory

2.1 Rock mass classification systems

Many systems have been developed for characterizing rock masses. Important contributors and the developed systems (in parenthesis) are listed here: Deere et al. (RQD), Wickham et al. (RSR), Bieniawski (RMR), Barton et al. (Q), Hoek & Brown (GSI) and Palmström (RMi).

Some systems like the Q-index is developed for estimating the need for tunnel reinforcement or stabilization, and others like the RQD and GSI are related to the general quality description of the considered rock mass or core specimens. The important systems in this report are the RQD, *rock quality designation* and the GSI, *geological strength index*. These are of importance, since tunnel mapping was conducted using these as main quality descriptors. Both will be presented briefly in the following.

2.1.1 The Rock quality designation - RQD

The RQD was originally developed as a mean of classifying cored rock. The RQD is defined as the length of core fragments longer than 10 cm relative to the total considered length, or more explicitely

$$RQD = \frac{1}{l_{tot}} \cdot \left(\sum_{l \geq 10\ cm} l_i \right) \qquad \text{eq. 1}$$

Where l_i [cm] is the length of core fragment i, and l_{tot} [cm] is the total considered length of the core segment. A factor 100 is omitted in the definition of the RQD; the RQD generally is given as the percentage, not the numerical value. The calculation principle of the RQD is seen in Figure 1.

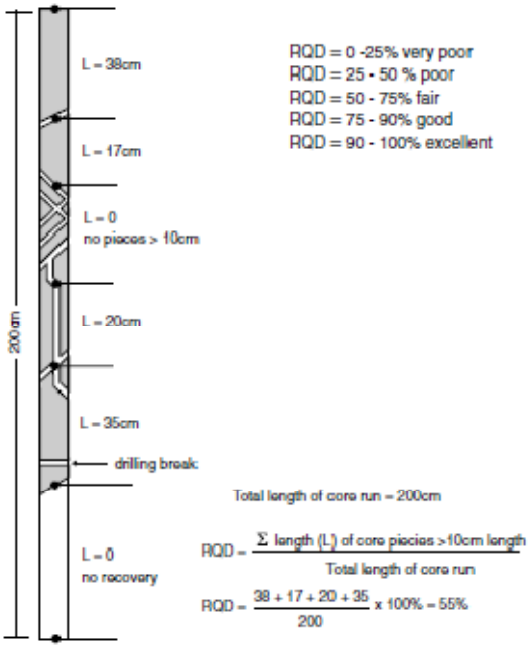

Figure 1: Calculation of the RQD. From Palmström (2005)

The RQD has some inherent drawbacks, which are illustrated in Figure 2. The figure shows that an RQD value of 0 can be assumed by a joint scenario which resembles both RQD = 0 and RQD = 100, where the RQD = 0 is evaluated for core fragments of length = 9 cm and the RQD = 100 is evaluated for fragments of length = 11 cm. Here only 2 cm of joint spacing dictates if the evaluation is the one or other extreme. The evaluation can further yield RQD = 100 value for core fragments of length = 11 cm and RQD = 100 for completely intact core segments.

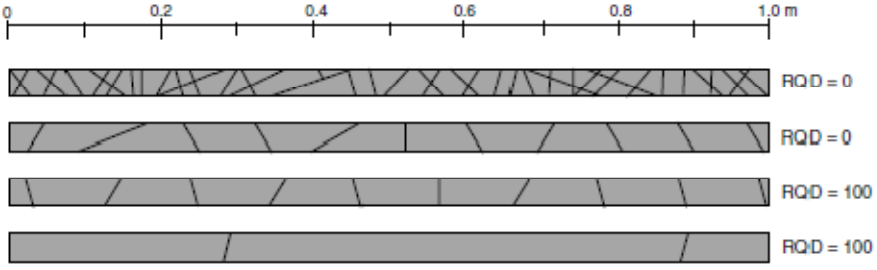

Figure 2: Similarities of RQD in dissimilar cores. From Palmström (2005)

Further is the RQD very directionally dependent, since joints parallel to boring will not be detected, even though they are present. So when applying the RQD for tunnelling, the poorest occurrence of rock in the considered tunnel section dictates the mapped RQD.

The RQD is related to intact and in situ p-wave velocities, $v_{p,insitu}$ and $v_{p,lab}$, by (from *Deere (1967)*)

$$RQD \approx 100 \cdot \left(\frac{v_{p,\,insitu}}{v_{p,\,lab}} \right)^2 \qquad \textbf{eq. 2}$$

The relation (eq. 1) and Table 1 states that for in situ velocities close to intact laboratory values will imply high rock qualities. The quality descriptions of Deere et al. are given in Table 1. Here F [m^{-1}] is the linear joint density, i.e. joints pr. meter.

Table 1: Ratios of sonic velocities and corresponding RQD values.

quality description	RQD [%]	F [m^{-1}]	$v_{p,insitu}/v_{p,lab}$ [-]	$(v_{p,insitu}/v_{p,lab})^2$ [-]
Very poor	0–25	>18	0–0.4	0–0.2
Poor	25–50	15–18	0.4–0.6	0.2–0.4
Fair	50–75	8–5	0.6–0.8	0.4–0.6
Good	75–90	5–1	0.8–0.9	0.6–0.8
Excellent	90–100	1	0.9–1.0	0.8–1.0

2.1.2 The Geological strength index – GSI

The GSI can be evaluated from the diagram in Figure 3. The GSI is evaluated by the visual joint patterns on a free surface, as depicted in the diagram, and from the condition of the joint wall surface. The GSI ranges from 100 for very massive, good quality rock to 0 for very laminated and sheared rock masses.

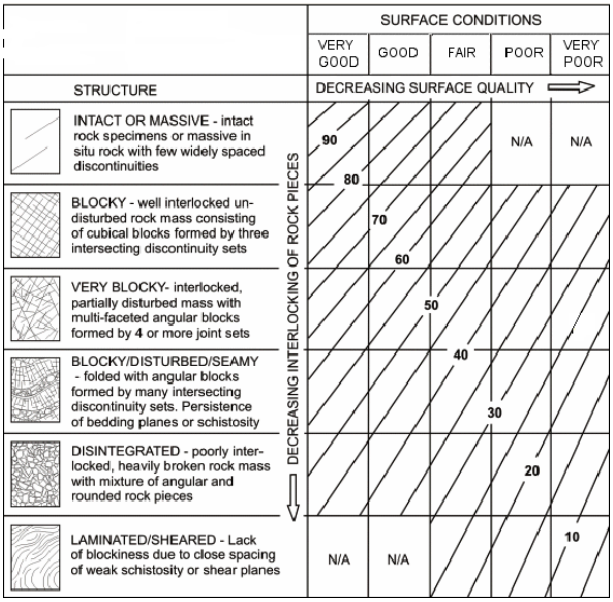

Figure 3: Evaluation of the GSI. From Hoek (2006)

The GSI was developed in the context of the Hoek-Brown failure criterion for intact rock, facilitating the formulation of the generalized Hoek-Brown failure criterion for jointed rock masses. The index is used to reduce the properties of the intact rock, which leads to a failure criterion describing the observed or mapped rock mass.

This is the strength of the GSI, that it is coupled to a widely utilized failure criterion, which make evaluations of rock masses possible in a formalized engineering sense. The primary weakness lies in the more or less subjective evaluation of the parameter.

2.1.2.1 The generalized Hoek-Brown failure criterion

The following sums up from *Hoek et al. (2002)* and *Hoek (1983)*.

The generalized Hoek-Brown (HB) failure criterion for rock masses is formulated as

$$\sigma_1 = \sigma_3 + \sigma_{ci} \cdot \left(m_b \cdot \frac{\sigma_3}{\sigma_{ci}} + s \right)^a \qquad \textbf{eq. 3}$$

Where σ_1 [MPa] and σ_3 [MPa] are the major and minor principal stresses, σ_{ci} [MPa] is the unconfined compressive of intact rock, m_b [-] and s [-] are reduced material parameters , and a [-] is a rock mass parameter.

The failure criterion is *non*-linear.

The parameter m_b [-] is given by the expression

$$m_b = m_i \cdot \exp\left(\frac{GSI - 100}{28 - 14 \cdot \mathrm{D}} \right) \qquad \textbf{eq. 4}$$

Where m_i [-] is a material parameter, which in the HB-criterion is analogous to the friction angle ϕ. For intact, hard igneous and metamorphic rock, the parameter assumes values of approximately 25-30.

The parameter s [-] is given by the expression

$$s = \exp\left(\frac{GSI - 100}{9 - 3 \cdot \mathrm{D}} \right) \qquad \textbf{eq. 5}$$

The parameter s is analogous to the internal cohesion c_o, *Hoek (1983)*, and equals 1 for intact rock.

The parameter a [-] is given by the expression

$$a = \frac{1}{2} + \frac{1}{6} \cdot \left(\exp\left(-\frac{GSI}{15} \right) - \exp\left(-\frac{20}{3} \right) \right) \qquad \textbf{eq. 6}$$

The parameter D [-] in the above is a disturbance factor which takes into consideration the effects of excavation to the strength of the considered rock, where D=0 for undisturbed excavations and D=1 for extremely disturbed rock masses. The HB-formalism further enables for estimation of rock mass deformation modulus and compressive strength. These are given by

$$E_m = \left(1 - \frac{\mathrm{D}}{2} \right) \cdot \sqrt{\frac{\sigma_{ci}}{100}} \cdot 10^{\frac{(GSI - 10)}{40}} \qquad \textbf{eq. 7}$$

$$E_m = \left(1 - \frac{\mathrm{D}}{2} \right) \cdot 10^{\frac{(GSI - 10)}{40}} \qquad \textbf{eq. 8}$$

for σ_1 [MPa] < 100 and σ_1 [MPa] > 100, respectively.

$$\sigma_{cm} = \sigma_{ci} \cdot \frac{m_b + 4 \cdot s - a \cdot (m_b - 8 \cdot s) \cdot \left(\frac{m_b}{4} + s \right)^{a+1}}{2 \cdot (1 + a) \cdot (2 + a)} \qquad \text{eq. 9}$$

This failure criterion will be used on the pressure tunnel.

2.2 Linear elastic theory and sonic wave propagation in hard rock

In the following some general theoretical concepts concerning the nature of sonic waves are presented briefly. The references are *Mavko, Mukerji & Dvorkin (2003)* and *Barton (2007)*. The theory is presented to give the reader a basic understanding of the propagation and nature of sonic waves.

Consider a homogenous, isotropic half space of well defined physical properties. In this medium two general classes of mechanical waves, i.e. with no net transfer of material, or stress transients can exist, namely body waves and surface waves. Body waves propagate through the interior or bulk of the medium, whilst surface waves are confined to propagate along the surface of the medium, or more generally along the interface of media with differing physical properties.

Body and surface waves can further be subclassified into wave types for which the mode of *particle motion* are qualitatively dissimilar. Here a distinction is made between the *direction of propagation* and the *direction of particle motion*, where the direction of propagation is directly related to the direction of energy flux and the direction of particle motion relates to the direction of the oscillational amplitude of the wave disturbance. Two essentially different types of waves are of importance, being longtitudinal (or compressional/dilational or p-wave) and transverse (or shear or s-wave) waves. The adjectives *longtitudinal* and *transverse* describes the direction of particle motion with respect to direction of propagation: for p-waves the direction of particle motion is parallel with the direction of propagation, and oscillating uniaxially between compressional and dilational strain, whilst for s-waves the direction of particle motion is perpendicular to the direction of propagation, see Figure 4.

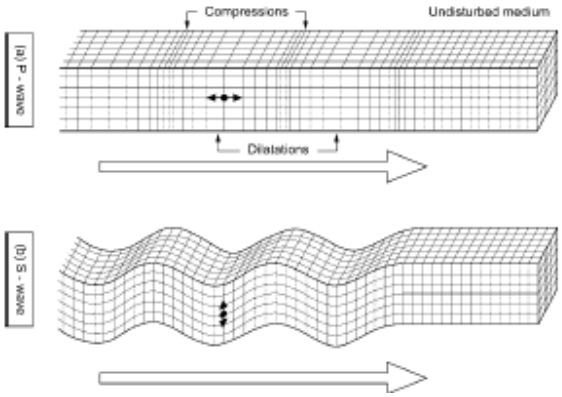

Figure 4: particle motion in p- and s-waves. From Barton (2007).

Since the wave amplitude of p-waves are parallel to the direction of propagation, the elastic nature is accordingly compressional. For s-waves the elastic nature is shearing, due to the fact that particle and propagation directions are perpendicular. Further, since it is usually assumed that the strains associated with sonic or seismic waves are of minute magnitude when being far away from the source, can these strains be considered to lie inside the elastic regime. The relations expressing the different linear elastic parameters for homogenous, isotropic media are shown in Table 2.

Table 2: Linear-elastic parameters. From From http://en.wikipedia.org/wiki/Elastic_moduli. Retrieved 05-04-2009.

	(λ, G)	(E, G)	(K, λ)	(K, G)	(λ, ν)	(G, ν)	(E, ν)	(K, ν)	(K, E)	(M, G)
$K =$	$\lambda + \frac{2G}{3}$	$\frac{EG}{3(3G-E)}$			$\lambda\frac{1+\nu}{3\nu}$	$\frac{2G(1+\nu)}{3(1-2\nu)}$	$\frac{E}{3(1-2\nu)}$			$M - \frac{4G}{3}$
$E =$	$G\frac{3\lambda+2G}{\lambda+G}$		$9K\frac{K-\lambda}{3K-\lambda}$	$\frac{9KG}{3K+G}$	$\frac{\lambda(1+\nu)(1-2\nu)}{\nu}$	$2G(1+\nu)$		$3K(1-2\nu)$		$G\frac{3M-4G}{M-G}$
$\lambda =$		$G\frac{E-2G}{3G-E}$		$K - \frac{2G}{3}$		$\frac{2G\nu}{1-2\nu}$	$\frac{E\nu}{(1+\nu)(1-2\nu)}$	$\frac{3K\nu}{1+\nu}$	$\frac{3K(3K-E)}{9K-E}$	$M - 2G$
$G =$			$3\frac{K-\lambda}{2}$		$\lambda\frac{1-2\nu}{2\nu}$		$\frac{E}{2(1+\nu)}$	$3K\frac{1-2\nu}{2(1+\nu)}$	$\frac{3KE}{9K-E}$	
$\nu =$	$\frac{\lambda}{2(\lambda+G)}$	$\frac{E}{2G} - 1$	$\frac{\lambda}{3K-\lambda}$	$\frac{3K-2G}{2(3K+G)}$					$\frac{3K-E}{6K}$	$\frac{M-2G}{2M-2G}$
$M =$	$\lambda + 2G$	$G\frac{4G-E}{3G-E}$	$3K - 2\lambda$	$K + \frac{4G}{3}$	$\lambda\frac{1-\nu}{\nu}$	$G\frac{2-2\nu}{1-2\nu}$	$E\frac{1-\nu}{(1+\nu)(1-2\nu)}$	$3K\frac{1-\nu}{1+\nu}$	$3K\frac{3K+E}{9K-E}$	

Notice that any linear elastic parameter can be calculated if two others are known.

These considerations give rise to the following relations for body waves, derived from classical linear elastic theory and thermodynamics:

$$M_{dyn} = \rho \cdot v_p^2 \Rightarrow v_p = \left(\frac{M_{dyn}}{\rho} \right)^{\frac{1}{2}} \quad \textbf{eq. 10}$$

$$G_{dyn} = \rho \cdot v_s^2 \Rightarrow v_s = \left(\frac{G_{dyn}}{\rho} \right)^{\frac{1}{2}} \quad \textbf{eq. 11}$$

Here the subscript *dyn* corresponds to *dynamical* values, opposite to *static* values. Dynamically induced stresses are transient i.e. of small temporal extent, whereas statically induced are long-term. Dynamical stiffnesses are in general larger than static stiffnesses, i.e. if a general linear elastic parameter is termed S, then

$$S_{stat} < S_{dyn} \quad \textbf{eq. 12}$$

Utilizing $M = K + \frac{4}{3}G$ one can compute

$$v_p = \left(\frac{K_{dyn} + \frac{4}{3}G_{dyn}}{\rho} \right)^{\frac{1}{2}} \quad \textbf{eq. 13}$$

This relation illustrates the inherently faster nature of p-waves relative to s-waves, since M always will be numerically larger than G for a given (solid) medium. Fluids cannot act as a medium for shear waves, because of their incapability to transfer shear stresses.

A dynamic Young's modulus can be calculated as, *Barton (2007)*

$$E_{dyn} = \rho \cdot v_p^2 \cdot \frac{\left(1 + \nu_{dyn}\right) \cdot \left(1 - 2 \cdot \nu_{dyn}\right)}{\left(1 - \nu_{dyn}\right)} \qquad \textbf{eq. 14}$$

Surface waves are often categorized as Rayleigh and Love waves. Rayleigh waves, often called ground roll or SV-waves, are surface shear waves for which the particle motion is perpendicular to the the surface or interface, and Love waves are surface shear waves, often termed SH-waves, which oscillate in the same plane as the surface/interface. Se Figure 5.

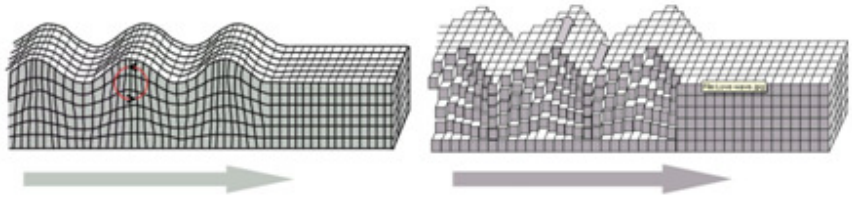

Figure 5: Particle motion in surface waves. Rayleigh waves to the right, and Love waves to the left. From http://en.wikipedia.org/wiki/Seismic_wave.

Rayleigh waves relevant to geotechnicians, since new inversion methods utilize that Rayleigh waves are dispersive or frequency dependent. This dispersive nature can give valuable information about overburden properties when applying a method called *spectral analysis of surface waves* (SASW). Here the paper of Nazarian & Stokoe (1983) is of importance, but applying the method lies outside the scope of this thesis.

2.3 Sonic velocities and geology

In this section the interplay between geology and sonic velocities will be presented briefly, i.e. how geology effects sonic velocity as a hard rock quality descriptor, with *Barton (2007)* as main reference.

2.3.1 Expected sonic velocities in hard rock

In general a manifold of *naturally occurring* factors influence sonic velocities in hard rock, namely (in unprioritized order) joint frequency (quantified for example by RQD), porosity, rock strength, density, in situ stress (depth), anisotropy, degree of fluid saturation and weathering etc. These factors can interact and be dependent on each other, forming a complex key for evaluating gathered sonic data.

The qualitative effects of the above mentioned natural factors are shown in Table 3.

Table 3: Factors influencing p-wave velocity in hard rock

influencing factor	***higher** velocity if*	***lower** velocity if*
fracture/joint density	low	high
strength/stiffness	high	low
degree of weathering	low	high
hydraulic permeability	low	high
density	high	low
porosity	low	high
temperature	low	high
# of frost cycles	small	large
depth (in situ stress)	large	shallow
water saturation	high	low

Further will the process of excavation introduce mechanically induced changes in the rock mass, which also influence the p-wave velocity. When using blasting as the excavation method, the rock mass will locally be disturbed by the by the extreme stresses produced at detonation. *Barton (2007)* refers to the effected zone as the *excavation disturbed zone*, or EDZ. The blasting process can form microcracks in the rock grain structure as well as visible fractures in the rock, which affect the velocities negatively. This effect is seen in Figure 6.

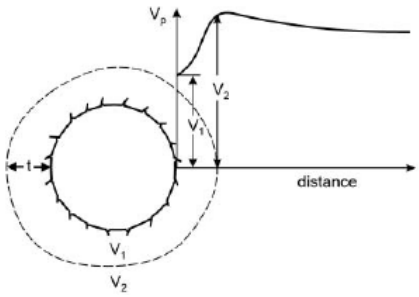

Figure 6: The EDZ and radial sonic velocity gradient.

From Barton (2007)

The figure shows a circular excavation and the qualitative velocity changes observed near the EDZ. The radial velocity gradient has a minimum at the excavation surface, which rises to a maximum at a given distance t from the surface, which asymptotically reaches the undisturbed velocity. This effects is of importance to this report, since seismic measurements during field investigations were carried out in such an EDZ.

For intact, unweathered hard rock a range of p- and s-wave wave velocities are expected, as shown in Table 4 , where relevant rock types to this report are highlighted.

Table 4: Expected sonic velocities in different materials.

From Barton (2007)

Material	v_p [m/s]	v_s [m/s]
Alluvium	500-2100	
Clay	1100-2500	
Sand	200-2000	
Glacial Till	***400-1700***	
Sandstone	1400-4500	
Shale, Slate	2300-4700	
Limestones		
Soft	1700-4200	
Hard	2800-6400	
Crystalline	5700-6400	
Dolomite	3500-6900	
Granite, Granodiorite	***4600–6000***	***2800–3200***
Diabase	5800–6000	
Gabbro	6400–6700	3400–3600
Basalt	5400–6400	2700–3200
Schist	4200–4900	2500–3200
Gneiss	***3500–7500***	***3300–3700***
Mica gneiss	**5500-5800**	
Water	***1450***	
Ice	***3840***	
Air	335	

Notice the large range of p-wave velocities for gneiss. This fact can be explained by the wide differences in density and mineralogical composition of this rock type. The range of sonic velocities for glacial till is explained by the dependence on degree of consolidation and gradation, and thereby density.

Eventhough no s-wave data were collected during the field investigations, some relations regarding this will be presented to give a sense of how this velocity can give further information about the considered rock mass.

In general, for jointed hard rock, the ratio of v_p and v_s will lie in the range from 1.80 for sparsely jointed rock to 1.89 for heavily jointed, *Barton (2007)*:

$$1.80 \leq \frac{v_p}{v_s} \leq 1.89 \qquad \textbf{eq. 15}$$

For intact, zero-porosity hard rock, the ratio of v_p and v_s will assume the value approximately that of √3, *Barton (2007)*.

The almost constant ratio of v_p to v_s is supported well by the following Figure 7, where an approximate proportionality is seen between v_s versus v_p for a range of different hard rock types, *Barton (2007).*

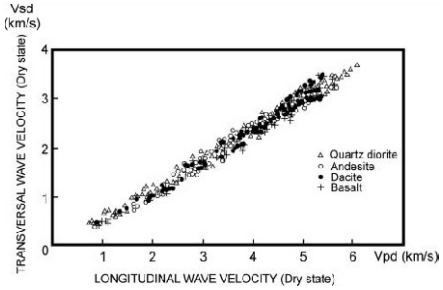

Figure 7: Relationship between p- and s-wave velocities. From Barton (2007)

The ratio of v_p and v_s is further related to the dynamic Poisson's ratio ν_{dyn} by the following relation

$$\frac{v_p}{v_s} = \left(\frac{2 - 2 \cdot \nu_{dyn}}{1 - 2 \cdot \nu_{dyn}} \right)^{\frac{1}{2}} \qquad \textbf{eq. 16}$$

Solving for ν_{dyn} yields

$$\nu_{dyn} = \frac{1}{2} \cdot \frac{\left(\frac{v_p}{v_s} \right)^2 - 2}{\left(\frac{v_p}{v_s} \right)^2 - 1} \qquad \textbf{eq. 17}$$

Note that this relation in *Barton (2007, p. 7 equation 1.6)* is erroneously typed as

$$\nu_{dyn} = \frac{\left(\frac{v_p}{v_s} \right)^2 - 2}{2 \cdot \left(\frac{v_p}{v_s} \right)^2 - 1} \qquad \textbf{eq. 18}$$

Inserting the values for the ratio of v_p to v_s of √3, 1.80 or 1.89, respectively, yields

$$\nu_{dyn} = 0.250 \quad \vee \quad \nu_{dyn} = 0.278 \quad \vee \quad \nu_{dyn} = 0.301$$

Dynamic Poisson's ratio thereby assumes larger values for more heavily jointed scenarios, or equivalently when sonic velocities are low. For unconsolidated, near-surface sediments, the ratio v_p to v_s actually can assume values of 20 to 40, yielding Poisson's ratios greater than 0.45, *Barton (2007)*. For intact rock, with ν_{dyn} = 0.250, a rough conversion from the dynamic modulus of uniaxial strain M_{dyn} to dynamic Young's modulus E_{dyn} is done by multiplying M_{dyn} with the factor

$$\frac{\left(1 + \nu_{dyn}\right) \cdot \left(1 - 2 \cdot \nu_{dyn}\right)}{\left(1 - \nu_{dyn}\right)} \qquad \textbf{eq. 19}$$

Inserting the value ν_{dyn} = 0.250 for intact rock yields

$$E_{dyn} = 0.833 \cdot M_{dyn} \qquad \textbf{eq. 20}$$

So by determining the sonic velocities and the density of the medium in which sonic waves, an understanding of the elastic nature can be obtained. It is the aim to couple these dynamic properties with the static properties from compressive testing.

For more theory on the effects of geology on v_p see enclosure 1.

3 Field investigations

Field investigations were carried out at the Tasersuaq hydropower project near Sisimiut, Greenland. The investigations include refraction seismic surveys, Schmidt rebound measurements, engineering geological mapping and sampling rock specimens for laboratory testing.

In the following location, climate, geology will be presented.

3.1 Location and climate

The hydropower project is located on the west coast of Greenland at approximately 67° 7' N and 53° 20' W, and is thereby situated roughly 70 km north of the arctic circle.

In the zoomed map, the *approximate* tunnel trace is seen. The coast line lies immediately outside the zoomed map, in the western direction.

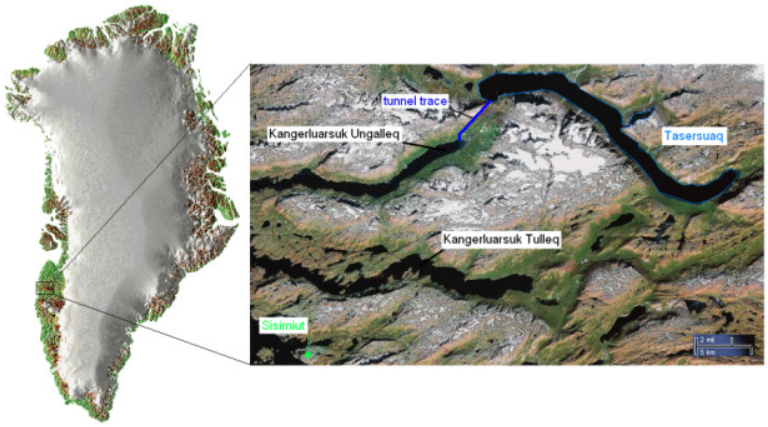

Figure 8: Overview map. From Google Maps, retrieved 06-05-2009.

In enclosure 2 the a map over the project area is seen, including the positions of the sites where field investigations was carried out. These are referred to the *access/maintenance tunnel*, from station 0 m to station 100 m, and the *pressure tunnel* site. The enclosure further includes the geospatial basis for the geocoded map. The enclosure 2 describe some main details about the hydropower project at Tasersuaq.

The climate is arctic with mean annual temperatures as shown below in Table 5 and Table 6. The climate data has been collected by Asiaq (The Greenland Survey), and can be found on the webpage www.asiaq.gl. Data from Tasersuaq are based on observations from June 1st 1980 to December 31st 2005, and from October 1st 1991 to December 31st 2005 for Sisimiut-data.

Table 5: Climate data for Tasersuaq.

month	Jan	Feb	Mar	Apr	May	Jun	*Year*
mean temp [°C]	-16.2	-18.9	-17.3	-8.9	-1,0	4.7	
month	Jul	Aug	Sep	Oct	Nov	Dec	*-5.0*
mean temp [°C]	7.6	6.6	3.1	-2.4	-6.5	-11.3	

Table 6: Climate data for Sisimiut.

month	Jan	Feb	Mar	Apr	May	Jun	*Year*
mean temp [°C]	-12.7	-15.4	-13.6	-5.3	0.4	4.6	
month	Jul	Aug	Sep	Oct	Nov	Dec	*-3.6*
mean temp [°C]	6.8	6.6	3.5	-1,0	-5.6	-8.9	

The difference of 1.4 °C in the mean annual temperatures of the two locations, is due to the fact that Tasersuaq is placed further away from the coast, implying pronounced inland climate characteristics, i.e. not mediated as much by the waters of the Davis Strait as Sisimiut. As shown on Figure 9 Tasersuaq is placed near the transition between areas with continuous and discontinuous permafrost, *Humlum & Christensen (2000).*

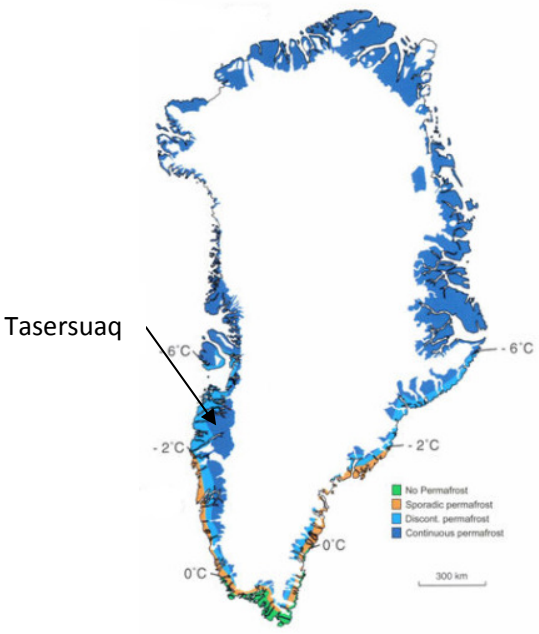

Figure 9: Map of permafrost distribution in Greenland. Humlum & Christensen (2000).

The climate data further show reason for taking into consideration that thawing of the active layer at Tasersuaq is delayed relative to the same occurence at Sisimiut. This effect is of relevance, if electromagnetic (EM) methods are applied in surveying the subsurface, since EM-signals are damped significantly in the presence of ice, opposite to the presence of water in liquid form, *Brandt (2008)*. This is due to the high resistivity ρ [Ωm] of ice relative to water, or conversely, due to the low specifik conductance σ [S/m] of ice relative to water, since, for a given material, ρ·σ=unity.

3.2 Regional bed rock geology of the Sisimiut area

3.2.1 The Nagssugtoqidian orogenic belt

The following outlines descriptions from *Henriksen (2005).*

The Tasersuaq area is part of the Nagssugtoqidian orogenic belt, which reaches from Kangerlussuaq in the south to Qeqertarsuup Tunua (Disko Bay) in the north, the orogen extends east under the Inland Ice Cap and reappears in the Tasiilaq area, East Greenland. The orogenic belt was generated by the collision of archaic continents.

The Nagssugtoqidian orogen is chiefly comprised of gneiss and granite with embedded, metamorphed, archaic (4.0-2.5 billion years old) sediments and vulcanic rocks. The geological age of the orogen itself is 1.79-1.65 billion years old, but younger intrusions of granite are encountered. Lineations are seen in a general east-west direction, of which amphibolitic bands are of geotechnical importance, due their relatively weaker properties, especially regarding the enhanced susceptibility to weathering of this rock type, Foged (1979). The dominant direction of lineation also appears in the general foliation strike trends in the bedrock.

3.2.2 Topographical features

The following is summarized from *Foged (1979)*.

The topography in the region is dominated by glacial erosion: large U-shaped valleys, skerries in the outer coastal areas, glacial and fluvial and marine deposits above and below current sea level; the submerged deposits, in the form of once peripheral morains, are in the waters of Sisimiut called the Great Halibut banks.

The Tasersuaq hydropower plant is constructed in a valley formed by glacial erosion; the U-shaped valley is directioned northeast-southwest, and glacio-fluvial and marine deposits are found in the lower parts of the valley.

The area has experienced major isostatic and eustatic sea level changes due to changes in ice cover extent and thickness; upper marine limits (UML) are seen in some areas to be in the magnitude of over 120 m above current mean sea level.

The high UML facilitates the possibility of encountering quaternary, marine deposits with sea shells at altitudes up to UML. Since glaciofluvial events, and other events causing fresh water flow, have leached out considerable amounts of the original salinity in the deposits, particularly clay deposits will be affected, since minor

mechanical disturbances of salt-leached out clays may induce liquefaction-like behaviour, i.e. very sensitive to quick clay. But this important, sediment related, subject is not within the scope of this report.

3.3 Previous investigations

The following summarizes observations reported in *GTO (1985)* concerning the geology at the Tasersuaq hydro power plant, based on surface mapping and surface refraction seismic surveys; the investigations further contained geoelectrical soundings and profiles and surveying including establishment of a reference elevation system, but these lie outside the scope of this report. A boring program was conducted in 1992, by Dansk Geoteknik A/S (English: Danish Geotechnics), this is also briefly summarized. Further will findings from the actual tunnel mapping performed during the excavation phase be presented. The tunnel mappings were performed by the contractor, Istak.

3.3.1 Surface mapping

In general, transitions in rock type adopt the directions of the lineations in the Nagsugtoqidian orogen, namely being subparallel and striking east-west. Foliation trends are in general recurring and follow the same strike trend, and dipping steeply to vertically. Several weakness zones are observed, and intersect the general lineation trend at an angle of approximately 45 degrees, and dipping 50-60 degrees south; these weakness zones are reported to be concentrated in the rock nearest to the lake. See enclosure 3 for a map showing the plane extents of the rock formations observed from surface mapping. The actual persistances of the observed weakness zones are not known, i.e. it is not known if they extent to intersect with the tunnel trace.

The bedrock in the western valley side above the tunnel trace placement, and nearest to the inlet, consists primarily of granodioritic to quartzdioritic gneiss. This rock transitions into a rock body shifting from gneiss to granite containing both quartz and biotite; this rock type is the most dominant along the tunneltrace. This rock type transitions into monzonitic/syenitic/biotite gneiss near the outlet, reported to have considerable biotite and amphibole content, and with low quartz content.

Weathering processes in the bed rock is reported to penetrate up to 20 m into the rock mass.

3.3.2 Borings

A total of 14 borings were carried out in June 1992, these are abbreviated B9201 through to B9214 included. The boring profile of B9201 is seen in enclosure 4. The profile includes, besides the geological core descriptions, core recovery percentages, linear (natural) joint density and RQD values. Overburden soils were not sampled, only geologically classified, including the eventual visual ice content. Some overview data from the borings are seen in Table 7.

Table 7: Previous borings from 1992.

boring ID	elevation [MSL]	boring depth [m]	depth to bedrock	RQD<50 top of bedrock
B9201	133.5	143.5	3.8	4
B9202	100.0	9.75	6.25	3.8
B9203	46.8	4.75	1	3.8
B9204	19.2	3.75	0.2	3.8
B9205	10.2	3.25	0.2	3.5
B9206	37.3	13	1.6	3
B9207	44.1	14.25	13	1
B9208	35.2	6	>6	NA
B9209	33.4	6	>6	NA
B9210	32.6	6	>6	NA
B9211	19.7	23.5	>23.5	NA
B9212	16.7	6	>6	NA
B9213	15.5	6	>6	NA
B9214	12.2	15.5	>15.5	NA

All borings to bedrock showed that the bedrock consists of biotitic gneiss with larger, pegmatitic microcline crystallizations. Depth to bedrock ranges from 0.2 m to greater than 23.5 m, since some borings do not reach bedrock. The borehole logs show that the depth of weathering from the top of bedrock is maximally 4 m, estimated by finding the depth to which RQD<50 corresponding to *poor* quality, *Deere et al. (1967)*; this distinction between weathered and fresh is the authors choice. It should be noted that some boring do not extend to cover the full weathering zone, but acts only as a mean of recognizing that bedrock has been reached. In the lower, more competent rock RQD values generally lie in the range from 70-95, corresponding to *good* to *excellent* quality. Core recovery values all lie within the range from 95-100 % when coring bedrock, where the core recovery value is the length of retrieved core relative to bored penetration.

Several borings encountered frozen sediments, indicating the presence of permafrost and the thickness of the active layer.

The borings B9201 to B9206 were carried out near the outlet/power house placement, which makes these most relevant to this report. The remaining borings were placed nearer to the lower parts of the valley.

Of these, the boring B9201 is the most interesting, since it reaches a final depth of 143.5 m below surface (m.b.s.), thereby intersecting the planned tunnel trace elevation. The boring reaches a weakness zone at approximately 43 m.b.s., or equivalently about 90 m above MSL. Here RQD decreases from 91 to 49, and near-vertical 'rusty' joints are reported in the log. The zone is roughly 2 m long in the direction of the boring, which is assumed to be vertical. The weakness zone is followed by a 2 m zone where RQD is 77, but still smaller than for the following rock mass, where RQD is about 90. The RQD=77 zone is reported to include slickensided joint walls, which can pose a reason mechanical instability when tunnelling. Strikes can not be determined from a single boring, so it it can not be determined if the zone extends to intersect the tunnel trace. Two additional deep boring could possibly encounter the same zone, which enables a geometrical estimation of the weakness plane's strike and dip.

The boring included subsequent point load tests series on samples from 20.5 m.b.s. to 141.6 m.b.s.. The mean axial point load indices ranged from 3.7 MPa to 5.4 MPa, and the mean diametric ranged from 2.3 MPa to 5.4 MPa. The mean (of the mean) values from axial and diametric tests are 4.2 MPa and 4.3 MPa, respectively, with corresponding standard deviations of 0.79 MPa and 1.4 MPa. See enclosure 5 for the original point load data. The anisotropy index between diametric and axial is 4.3MPa/4.2MPa=1.02, and is thereby nearly isotropic, when considering the mean of means.

3.3.3 Refraction seismic surveys

A total of 6 refraction seismic profiles were carried out, these are abbreviated S8501 through to S8506 included.

The profiles S8501, S8502, S8504 and S8505 are of shorter length than the profiles S8503 and S8506. The shorter profiles indicate p-wave velocities ranging from 4000-5600 m/s, further do they indicate overburden soil thicknesses ranging from 0-55 m, where the greatest thicknesses are encountered near the lower parts of the valley.

S8503 and S8506 are almost parallel and of lengths of 580 m and 425 m, respectively, and these are of most relevance, since they both indicate the presence of a weakness zone of lower sonic velocity, which could be the same in both profiles. They are further placed near the outlet, and measured bedrock velocities are those of the biotitic gneiss, which is also investigated in the field investigations in this project. The profiles are seen in enclosure 6.

The profiles S8503 and S8506 do in general predict p-wave velocities of 4200-5300 m/s for the more competent rock mass, and velocities of 3300 m/s for the encountered low-velocity weakness zones. The p-wave velocities in overburden soil are interpreted to be roughly 2000 m/s in general.

The method used to interpret the seismic data is the plus/minus method of *Haagedoorn (1959)*. This implies that the weakness zones only can be interpreted as *vertical* low-velocity regions, i.e. can no dips be evaluated from this method. Estimated, guessed dips of the low-velocity zones were drawn into the profiles on a later date during the actual hydropower project.

3.3.4 Tunnel mapping

The tunnel mapping was performed following the Q method for evaluation of needs for tunnel *stabilization*, being shotcrete and rock bolts; the method does not evaluate the rock mass strength. The Q method includes an evaluation of RQD, which in tuneling commonly is evaluated as a the *poorest* occurence of rock in the considered tunnel section, including the just excavated/blasted parts of the face, roof and both walls of the tunnel, but excluding fractures induced by excavation. Each mapping session covers a 10 m section of the tunnel. The floor is not relevant, since gravity here acts stabilizing, which is why it is not included in the Q-mapping sessions. Table 8 shows the mapped RQD and Q indices for the parts of the tunnels of interest in this report. The RQD and Q values are courtesy of Ístak Ltd.

Table 8: Tunnel mapping.

station [m]/site	RQD	Q index	GSI
0-10	75	5	-
10-20	75	5	72,5
20-30	80	13	77,5
30-40	80	9	77,5
40-50	80	9	77,5
50-60	80	9	82,5
60-70	85	9	85
70-80	85	17	75
80-90	80	9	80
90-100	80	12,8	80
pt	40	0,4	47,5

Here the stationing refers to the access/maintenance tunnel and 'pt' refers to the pressure tunnel site.

The GSI values from the logging performed in relation to this report are also shown for comparison.

All three quantities are dimensionless.

3.4 Methods and equipment

3.4.1 The plus/minus method

The method of interpreting the seismic data obtained during field investigations is here presented briefly. For a more rigorous presentation of the refraction seismic method, the reader is referred to enclosure 7. The following is referenced to *Reynold (1997)*.

To encompass complex refractor topographies, the plus/minus method of *Haagedoorn (1959)* can be utilized. This method cleverly handles undulating refractor topographies when assuming travel time reciprocity, that is, even though apparent refractor velocities differ from each other in a dipping/undulating refractor scenario, the absolute travel time in the forward and reverse directions must be equal, i.e. $t_{FR} = t_{RF}$. See Figure 10. The method is restricted to only being valid in the rafractive overlap, that is, only for first arrivals which have been critically refracted and therefore does the method not apply on direct waves from the upper layer.

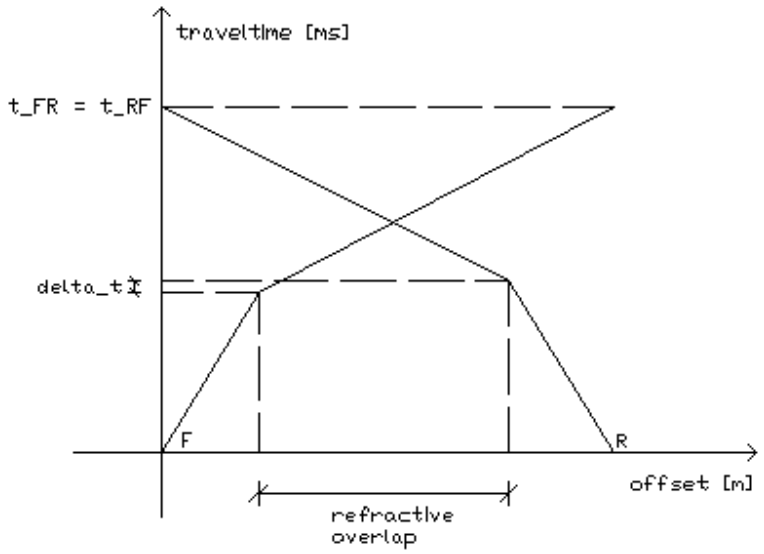

Figure 10: Forward and reverse travel time curves, and reciprocal travel times.

Given the travel times for first arrivals at each geophone G_n in both the forward and reverse directions, t_{nF} and t_{nR} and, the plus/minus method defines the *plus time term* t^+ and the *minus time term* t^- as

$$t_n^+ = t_{nF} + t_{nR} - t_{FR} \quad \textbf{eq. 21}$$

$$t_n^- = t_{nF} - t_{nR} - t_{FR} \quad \textbf{eq. 22}$$

The plus time term is used in refractor depth analysis, since

$$z_n = \frac{t_n^+ \cdot v_1 \cdot v_2}{2 \cdot \sqrt{v_2^2 - v_1^2}} \quad \textbf{eq. 23}$$

Where z_n [m] is the refractor depth under the considered geophone. The depth is measured perpendicularly from the refractor and up to the considered geophone.

The minus term is used in velocity analysis, since

$$v_2 = \frac{2}{m(t^-)} \quad \textbf{eq. 24}$$

Where $m(t^-)$ [s/m] is the slope of the best linear fit of the minus term versus geophone offset, since the t^- versus offset curve will be linear for a homogeneous and isotropic refractor.

An actual refraction seismic profile, being non-ideal, can be divided into segments of differing velocities by performing linear regression on only a part of the t^- curve. Since a t^- term for each geophone can be calculated, one can choose to evaluate the refractor sonic velocity by for example only considering two or more geophones at a time. The velocities can then be evaluated by

$$v_{2,AB} = \frac{2}{m(t_{AB}^-)} \quad \textbf{eq. 25}$$

Where the indices A and B refer to that linear regression should be performed on geophones between and including the offsets A and B. The division into velocity zones is shown on Figure 11. The figure shows 6 geophones and their corresponding t- versus offset curve. The corresponding velocities are seen on the velocity curve above, where the interval for evaluating v_2 is 1 geophone spacing, except between geophones G3 and G5 where the interval is two geophone spacings.

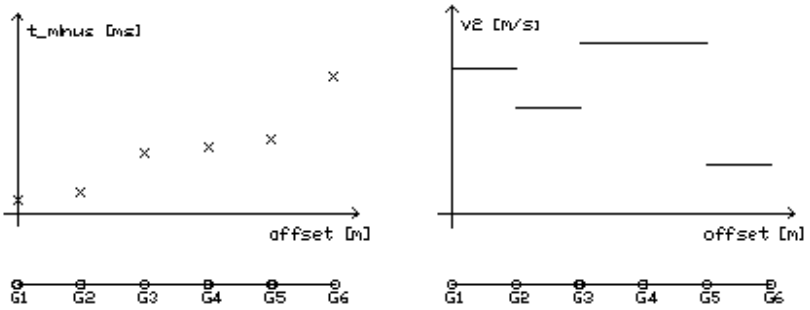

Figure 11: The t- term and velocity profile.

The velocity of the upper layer can be determined by linear regression on the travel time curves from the upper layer.

The method is very easily applied to the picked first arrivals.

3.4.2 Refraction seismic surveying

The refraction seismic surveys were conducted following the recommendations of the *ISRM Suggested Methods for Land Geophysics in Rock Engineering (2004)*.

Refraction seismic surveys were conducted in the access/maintenance tunnel from station 6 m to 96 m, and a single spread was surveyed in the pressure tunnel. The surveys were placed on the tunnel floor, where a layer of rock and soil was later spread out to enable driving with machinery in the tunnel. This layer was of a thickness lesser than 0.5 m, according to the attending personnel at the project site. The tunnel was open to the weather, only closed off by a temporary wooden port. This fact, together with the winter climate, meant that the temperature inside the access/maintenance tunnel was a couple of degrees below freezing, which is why the rock/soil fill on the tunnel floor was frozen. So the geophones could not be directly inserted, which meant that insertion holes were pre-drilled, which thawed the fill locally, and froze again after the geophones were inserted, and thereby ensuring good contact with the ground/floor.

For conducting the refraction seismic surveys a 4 channel seismograph (or oscilloscope) was used. The 4 geophones are connected to the oscilloscope individually with cables of lengths 3, 5, 7 and 9 m. This cable configuration lays a natural restriction on the maximum length of a single spread.

The oscilloscope was of the type *HandyScope HS4* from TiePie Engineering, see Figure 12, and is connected to a laptop via a serialport-to-USB(2.0) cable, and the instrument is powered through this connection. The instrument can sample with a frequency of up to 50 MHz, and a maximum record length of 2^{17}=131072 samples.

The driver software on the laptop is specialized and is named *HandyScope HS4 Version 2.85*, and includes multimeter, oscilloscope, spectrum analyzer and a transient recorder.

Figure 12: The 4-channel oscilloscope.

The used geophones were of type *Geo Space GS-20DX*. Specifications can be seen in enclosure 8. Figure 13 shows a picture of a single geophone. The geophone type is 1-component, and is only sensitive to movements perpendicular to the plane it is inserted into.

Figure 13: Geo Space GS-20DX geophone.

The triggering mechanism is comprised of the electrical circuit formed when a 2 kg hammer impacts a metal plate, where both hammer and plate are connected to the HS4 device.

Information about hardware and software can be found on the website of TiePie Engineering, www.tiepie.nl. From here can specifications and manuals can be downloaded.

3.4.2.1 Survey design

The survey configuration used during the field investigations was a 2 m geophone spacing, where only far sources were used, placed 2 m outside the spread. Both forward and reverse sources were utilized. Figure 14 shows the survey setup.

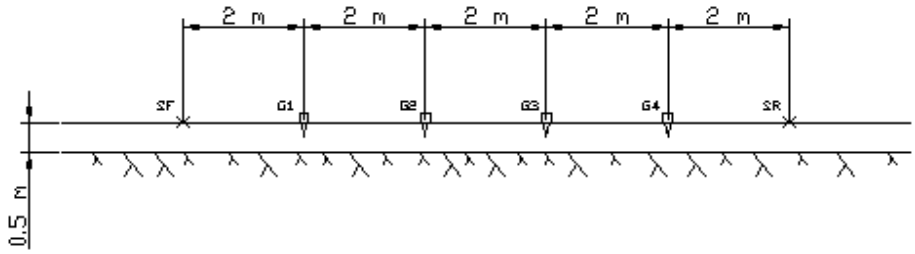

Figure 14: Used geophone spread.

On Figure 14 the sources are named SF and SR, corresponding to the forward and reverse directions for which they are respectively used. The geophones are named G1, G2, G3 and G4 in ascending order with respect to the positive offset direction.

The triggering mechanism did not function optimally, due to what is believed to be voltage transients in the electrical system, which is why stacking could not be used during surveys. The device is otherwise able of stacking a number of signals divisible by 2^n; if possible, 4 measurements would have been stacked for each source placement.

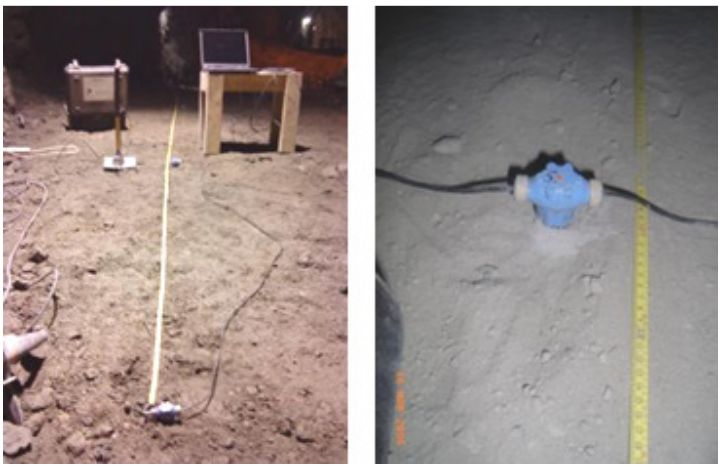

Figure 15: The setup realized during surveyng.

It is sought to be proven that the setup in Figure 14 produce first arrivals, which have been refracted, i.e. when considering the geophone nearest to the source, the first arrival will be a refracted ray, since these are the only data of interest. So in order to substantiate the geometrical design of the source-geophone setup, some assumptions were made. These include a planar two layer scenario, as shown on Figure 1 in enclosure 7, and that the minimum velocity in bedrock is 3300 m/s and the maximal velocity of the (frozen) rock/soil fill was 2000 m/s. The formula eq. 7 in enclosure 7 applies for the refracted arrival and the travel time of the direct ray can be calculated as 2m/(2000m/s) = 1.0 ms, since the distance between the source and nearest geophone is 2 m. The formula the travel time of the refracted ray, and this also yields 1.0 ms. Since the scenario above describes the least advantageous situation for a first arrival being the refracted ray, it is proven that the setup in Figure 14 yields the desired data. And since stacking of traces not was possible, it is also sought to maximize the signal

strength at the farthest geophone, relative to the source. Tests yielded that the configuration in Figure 14 yielded traces which were acceptable, when applying a gain of 10 to the farthest geophone channel.

During data acquisition a sampling frequency of 100 kHz and recording 1000 samples, and hence a sample length of $10^3/10^5$Hz=10 ms, and a temporal resolution of 1/100kHz=10µs is obtained. The choice of a sampling frequency and number of recorded samples is substantiated by assuming the minimal average sonic velocity along the spread encountered is 3000 m/s and knowing the distance between source and farthest geophone is 8 m. This gives rise to a maximum expected travel time of roughly 2.7 ms, which is lesser than the total recorded time window.

A fixed gain equal to unity was used, since the gain could be changed subsequently on each channel separately.

Once travel times for forward and reverse sources were recorded, the spread was moved further 4 m along the wished profile, thus leaving a 2 m overlap between spreads. Figure 16 shows the principle when moving the geophone spread; here spreads are offsetted for clarity and only 4 are shown. A total of 22+1 spreads were carried out, from station 6 m to 96 m.

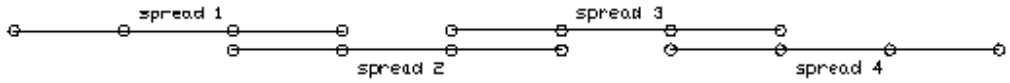

Figure 16: Overlap of spreads.

Since the trigger mechanism was noneffective, only relative travel times between the different geophones are determined. The time of first arrival at the geophone nearest to the source is dictated to represent the zero-time, to which first arrivals at the succeeding geophones are referenced to. This means that the total travel time t_{RF} from source to farthest geophone is not known, but if one considers the expression for the t^- term, it is seen that this total travel time t_{RF} is subtracted from each t^- term, which only changes the absolute values and not the relative values, meaning that the slope of the t^- terms versus offset is the same with or without the subtraction of t_{RF}. So when computing the t^- terms in the velocity analysis in this report, t^- equals t_{nF} minus t_{nR}, thus excluding the further subtraction of t_{RF}. Since this total travel time t_{RF} is not known, so refractor depths cannot be calculated, nor can the velocity of the upper layer be determined.

3.4.3 Schmidt rebound

The Schmidt rebound measurements were conducted in accordance with the *ISRM Suggested Method for Determining the Schmidt Hammer Rebound Hardness, revised version (2009).*

For measuring the Schmidt rebounds, a Proceq Schmidt hammer type N/NR was used. The hammer delivers on impact an energy of 2.207 Nm. Readings of the rebound values were precise to within 1 mm, according to the scale on the hammer. Figure 17 shows the actual model used. The hammer was new when used in the field investigations, and was therefore calibrated from the production site.

Figure 17: Proceq Schmidt hammer type N/NR.

L-type hammers are also available, but these deliver a smaller energy on impact, and are thereby sensitive to other ranges of hardnesses. Conversion from N-type to L-type rebounds, termed R_N [mm] and R_L [mm], respectively, is done via the following correlation, from the relevant *ISRM Suggested Method*.

$$R_L = \frac{R_N - 6.3673}{1.0646} \qquad \textbf{eq. 26}$$

The working principle of the hammer is that a spring loaded piston is released when the *plunger* is pressed against a surface. The plunger rebounds to an extent related to the recovered energy from the well defined impact energy stated above. The recovered energy is related to the hardness of the impacted material. The rebound magnitude in [mm] is the Schmidt rebound R.

The rebound is of course dependent on whether is works against or with gravity, i.e. being direction dependent with respect to horizontal. Rebounds in direction against the gravitational pull are smaller when impacting the same material and rebounding with the gravitational pull.

Schmidt rebounds correlate with other rock properties such as unconfined compressive σ_c [MPa] strength

$$\sigma_c = 1.45 \cdot e^{0.07 \cdot R_L} \qquad \textbf{eq. 27}$$

Correlations between Schmidt rebound and density, Young's modulus, p-wave velocity (and others) exist, but some not to a highly significant degree, making the conversion inaccurate. And only correlations between σ_c and Schmidt rebounds are explicitly given in the *ISRM Suggested Method*.

When performing rebound measurements two series of measurements were carried out, one series where impact were separated by at least one plunger diameter, and another where impacts were coincident. Each series is comprised of 20 individual rebound measurements. For both series, the mean, meridian, mode, minimum and maximum values are determined, and the impact direction both with respect to horizontal and eventual anisotropic features in rock are noted.

Measurements were carried out at 5 m intervals from station 6 m to 96 m along the access/maintenance tunnel. The pressure tunnel was also subject to a Schmidt rebound investigation, at the same place, as the refraction seismic investigation.

3.4.4 Engineering geological mapping

The mapping in the tunnels at the hydropower site was done following the *ISRM Suggested Method for the Quantitative Description of Discontinuities in Rock Masses (1978)*.

Mapped discontinuity features include orientation, spacing, persistance, roughness, wall strength, aperture, filling, seepage and number of sets. Further was the geological strength index GSI and the Joint Roughness Coefficient JRC_0 included in the mapping; JRC_0 is described in *Barton (2007)*.

During the mapping sessions in the field, a geological compass with built in clinometer was used. Dips and strikes of geological features were strike/dip measured to within 1^o according to the angle division on the clinometer. The type of compass used is shown on Figure 18. Further was a geological hammer used to evaluate rock hardness.

Figure 18: Geological compass with clinometer.

Since the tunnel surrounded the mapper, it was likely that magnetic minerals could effect the validity of strike measurements. To oblige to this, strikes were measured relative to the planar direction of the tunnel trace, the direction of increasing stationing being 'north'. A right hand rule was used to uniquely define strikes: the mappers right hand is placed *on* the desired discontinuity with the fingers pointing in the direction of dip (down dip), the thumb now point in the direction of strike. When using this convention the 'double' declarations like NE-SW or E-W are avoided. If, for example, a joint is dipping NE, then the NW-SE strike is simplified to only NW, when applying the rule. Of course the standard definition of strike was measured, the right hand rule only simplifies the notation in field. When seeing the tunnel from above, the clockwise direction was used as positive, when designating strikes a degree-value.

The mapping included the access/maintenance tunnel (from station 6 to 96) and a section of the pressure tunnel where refraction seismic and Schmidt rebounds were investigated.

4 Laboratory work

The following presents the principles and methods behind the laboratory work carried out at the Biulding & Construction School in Sisimiut. Conducted tests and measurements are presented, as are used equipment, test methods and principles of data analysis presented briefly.

4.1 Testing and measurement principles

4.1.1 Specimen preparation

To prepare the cored specimens and field samples a water-cooled, rotating rock saw was used to cut the core segments into the standard lengths for the different tests. When operating the saw safety goggles, ear plugs, gloves and an appropriate clothes were worn. Further was the saw equipped with an emergency stop button.

Figure 19: Rock saw.

Special care was put in to making the ends of the prepared specimens normal to the longtitudinal axis. This seemingly simple task proved to be difficultly executed, especially when handling specimens with a crosssection larger than that of an Ø 50 mm cylinder. The saw blade deflected when cutting the larger specimens, as was the sledge on which the specimens laid not fixated properly, and consequently did the ends not become normal to the longtitudinal axis nor parallel to each other, within the desired limits as described in the *ISRM Suggested Method for Determining the Complete Stress-Strain Curve for Intact Rock in Uniaxial Compression (1998)*.

When handling the saw it became possible to subjectively detect relative differences in rock hardnesses, since harder rock specimens obviously gives greater resistance than lesser hard when sawing through them.

4.1.2 Intact rock descriptions

Petrographical descriptions of intact rock were carried out following the conventions of the *ISRM Working Party, Lisbon, 1975*, which includes i: hardness, ii: degree of weathering, iii: ROCK TYPE (and colloquial name), iv: colour, v: texture (grain size), vi: fabric (equigranular/porphyritic/schistose/ foliate).

To understand the hardness classification used, the reader is referred to Table 9.

Table 9: Rock hardnesses. From ISRM, 1975.

class	hardness	field test
I	extremely hard	many blows with geologic hammer required to break intact specimen
II	very hard to hard	hand-held specimen breaks with hammer end of pick under more than one blow
III	moderate	cannot be scraped or peeled with knife, hand-held specimen can lie broken with single moderate blow with pick
IV	soft	can just be scraped or peeled with knife. Indentations 1–3 mm deep shown in specimen with moderate blow of pick
V	very soft	material crumbles under moderate blow with sharp end of pick and can be peeled with a knife, but is too hard to hand-trim for triaxial test specimen

The degree of weathering classification is seen in Table 10, ranging from fresh rock to residual soil.

Table 10: Weathering grade of rock. From ISRM, 1975.

grade	symbol	diagnostic features
fresh	F	no visible sign of decomposition or discoloration. Rings under hammer impact
slightly weathered	WS	slight discoloration inward from open fractures, otherwise similar to F
moderately weathered	WM	discoloration throughout. Weaker minerals such as feldspar decomposed. Strength somewhat less than fresh rock, but cores cannot be broken by hand or scraped by knife. Texture preserved
highly weathered	WH	most minerals to some extent decomposed. Specimens can be broken by hand with effort or shaved with knife. Core stones present in rock mass. Texture becoming indistinct but fabric preserved
completely weathered	WC	minerals decomposed to soil but fabric and structure preserved (saprolite). Specimens easily crumbled or penetrated
residual soil	RS	advanced state of decomposition resulting in plastic soils. Rock fabric and structure completely destroyed. Large volume change

The texture or grain grain classification is seen in Table 11, which ranges from very coarse grains larger than 2.0 mm, to very fine grains smaller than 0.06 mm. Further an amorph texture can be encountered, showing no individual grains, only a homogeneous mass, for example obsidian.

Table 11: Rock texture formulated as grain size. From ISRM, 1975.

class	size [mm]	recognition
very coarse grained	>2.0	grains measurable with ruler
coarse grained	0.6-2.0	clearly visible to naked eye
medium grained	0.2-0.6	clearly visible with hand lens
fine grained	0.06-0.2	just visible with hand lens
very fine grained	<0.06	not distinguishable with hand lens

Other descriptions were made following geological handbooks with description of different rock types. Here mainly *Henriksen (2005)* was used.

4.1.3 Bulk density and geometrical dimensions

The bulk density of regular shaped cored specimens was determined by geometrical volume calculations and weighing on a scale with a resolution of at least 0.01 g for smaller specimens and 1 g for larger. When measuring the geometric dimensions of the specimens a Vernier calliper with a resolution of 0.05 mm was used, see Figure 20.

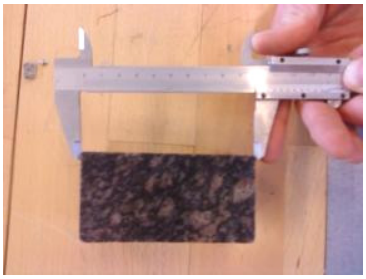

Figure 20: Dimension measurement with Vernier-calliper.

All measurements of dimensions during the the laboratory work, were carried out using a Vernier-calliper, and the number of measurements of each specific dimension was always 4.

For regular cylindrical specimens the bulk density ρ_{bulk} [g/cm^3] is calculated as

$$\rho_{bulk} = \frac{m_{air}}{\frac{\pi}{4} \cdot d^2 \cdot h} \qquad \textbf{eq. 28}$$

Where m_{air} [g] is the mass of in air, d [cm] is the diameter and h [cm] is the heght.

The bulk density of irregularly shaped specimens, e.g. having a piece chipped of, is determined using the principle of Archimedes utilizing the buoyancy of a, in deioninized water, submerged specimen to calculate its volume. The mass is determined by simple scale weighing within an accuracy of 0.01 g. The bulk density ρ_{bulk} [g/cm^3] is calculated as

$$\rho_{bulk} = \frac{m_{air}}{\left(\frac{m_{bouyant}}{\rho_{water}} \right)} \qquad \textbf{eq. 29}$$

Where m_{air} [g] is the mass of in air, $m_{bouyant}$ [g] is bouyancy when submerged in deionized water and ρ_{water} [g/cm^3] is the density of deionized water, which is 1.00 g/cm^3.

4.1.4 Determination of p-wave velocity

The determination of the p-wave velocity was done using the *ISRM Suggested Method for Determining Sound Velocity* as reference.

To determine the compressional wave velocity, a setup is used, as shown in Figure 21. A testing apparatus called a *PUNDIT*, an acronym for *portable ultrasonic non-destructive digital indicating tester*, is used to determine sonic travel times of generated sonic pulses. The device has a temporal resolution of up to 0.1 µs when calibrated satisfactory.

The signal generator in the PUNDIT produces an electrical pulse of a certain wave form, which, by a piezoelectrical, transmitting transducer, Tx, is converted into an ultrasonic pulse of frequency f=54 kHz, triggering the start of a temporal sampling. The sonic wave propagates through the specimen with the velocity v_p, and arrives at a receiving transducer, Rx, that converts the sonic wave into an electrical pulse, and triggering the temporal sampling to stop. The traveltime of the sonic pulse, Δt, being the length of the temporal sample, is digitally displayed on the PUNDIT unit. The PUNDIT is only triggered by a first arrival, so no later arrivals will be detected.

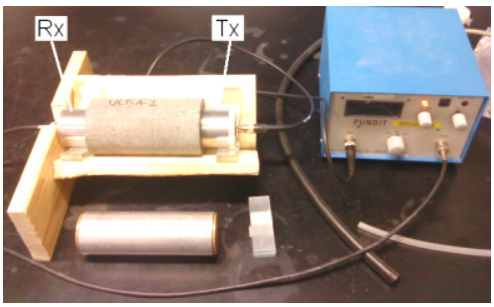

Figure 21: PUNDIT setup for intact p-wave velocity determination.

Before measuring, the PUNDIT is calibrated. First it is showed that a zero-distance reading actually reads zero traveltime on the display. This is achieved by placing the transducers in direct contact with each other. Afterwards the metallic, cylindrical, calibration specimen of well defined travel time, Δt=26.3 µs, is placed between the transducers, and the reading on PUNDIT display is manually set to the travel time of 26.3 µs, and thus achieving calibration.

The *ISRM Suggested Method* recommends that the specimen dimension normal to the wave propagation is at least 10 times the wave length of the sonic pulse. Since the frequency of the pulse is 54 kHz, and p-wave velocities generally were found to be in the range of 4000 m/s to 6000 m/s, the corresponding wave lengths become

$$\lambda = \frac{4000\frac{m}{s}}{54000\,Hz} = 0.074\,m \vee \lambda = \frac{6000\,\frac{m}{s}}{54000\,Hz} = 0.111\,m$$

Dictating the following minimal specimen 'diameters'

$$d = 0.74\,m \vee d = 1.11\,m$$

This calculation leads to considerations regarding if the governing elastic modulus of the p-wave velocity actually, in this case, is the modulus of uniaxial strain, or if the governing modulus in fact is Young's modulus, due to the lack of sufficient confinement perpendicular to the direction of propagation. The *ISRM Suggested Method* on the subject suggests that a frequency between 100 kHz and 2 MHz is used to determine the p-wave velocity. This frequency range produce smaller wavelengths, and thereby the relative conefinement is larger. So in the context of this report, the laboratory measurements of the p-wave velocity are assumed to be related to the dynamic Young's modulus E_{dyn}. This could not be stated directly in the *ISRM Suggested Method*.

To determine the travel time 10 consecutive measurements were made, switching the position of transducer and receiver after 5 measurements. Each measurement was performed by bringing the transducer-reciver pair in contact with the specimen, noting the travel time, and removing the transducer-receiver pair to begin a new measurement. The final travel time is the average of the 10 individual measurements. The p-wave velocity v_p [km/s] is calculated as

$$v_p = \frac{l}{\Delta t} \qquad \textbf{eq. 30}$$

Where l [mm] is the length of the specimen in the direction of the p-wave propagation or equivalently the distance between the transducer-receiver pair, and Δt [μs] is the travel time of the p-wave through the specimen.

A specimen from both series E and D were tested with the PUNDIT after being evacuated submarged in water for approximately 24 hours, and again after being dried for another 24 hours in a heating oven at 105 ^{o}C. This was done to show the effects of water saturation on the p-wave velocity.

Samples from the field work were prepared with the rock saw, such that two parallel planes at each end of the sample was obtained. The distance between these parallel ends were measured four times, at four different places on the sample. The arithmetic average of the four distances were used in later calculations of the p-wave velocity.

The transducers were sensitive to the ammount of sonic gel applied to the specimen ends. If the transducers were not pressed hard against the specimen ends at measurement start, the gel does not distribute and forms a layer between the specimen and the transducer, which delays the compressional wave arrival. The *ISRM Suggested Method for Determining Sound Velocity* recommends that a force of 10 N/cm^2 (≈1 kg/cm^2) is applied to the transducer-receiver pair.

4.1.5 Point load index

The point load testing was carried out following the *ISRM Suggested Method for Determining Point Load Strength (1984)*, to which the reader is referred to for the general theory.

The test specimen is not restricted by any requirements to form, both regular cylinders or blocks and irregular shaped specimens can be tested and assigned a point load strength, since the test simply applies a co-linear (failure) point force P [N] on a test specimen, which has a given minimal equivalent crosssectional area $(D_e)^2$ [mm^2], which geometrically coincides with the points where the force is applied, along which the specimen is assumed to fail.

To obtain an index value of the point load strength, a size correction to D_e = 50 mm must be performed. The most reliable method of size correction is done by plotting log(P) versus log($(D_e)^2$). This plot should ideally yield a linear trend with slope m. Linear regression yields an expression for the best linear fit, into which $(D_e)^2 = 50^2$ mm^2 is inserted.

$$\log(P) = m \cdot \log\left(D_e^2\right) + b \qquad \textbf{eq. 31}$$

The obtained value log(P_{50}) determines the size corrected $I_{s(50)}$ as [10^log(P_{50})]/50^2.

The point load index $I_{s(50)}$ [MPa] is then defined as

$$I_{s(50)} = \frac{P_{50}}{(50\,mm)^2} \qquad \text{eq. 32}$$

Where P50 [N]Further can a point load strength anisotropy index, $I_{a(50)}$, be evaluated for intact rock with anisotropic features, like foliation or schistose trends. The point load anisotropy index is the ratio between point load strength indices obtained from tests perpendicular and parallel to weakness planes, respectively, or more general, the ratio between maximum and minimum value of point load strength indices in two different, not necessarily mutually perpendicular, loading directions. Isotropic rock will have an anisotropy index close to unity, and anisotropic rock will have higher values.

$I_{s(50)}$ correlates proportionally to the uniaxial compressive and tensile strength; specifically, the mean ratio between uniaxial compressive strength and point load strength index is 20 to 25, and the ratio between tensile strength (uniaxial or Brazilian) and point load strength index is in mean 1.25. The ratios can be written as

$$\frac{\sigma_c}{I_{s(50)}} = 20 \textbf{ to } 25 \qquad \textbf{eq. 33}$$

$$\frac{\sigma_t}{I_{s(50)}} = 1.25 \qquad \textbf{eq. 34}$$

Ten or more measurements should be performed for satisfactory determination of $I_{s(50)}$. The value of $I_{s(50)}$ is calculated as the mean of the point load strengths of which the two highest and lowest values are discarded. If lesser than ten test are performed, only the single highest and lowest values are to be omitted in the calculation of the mean. The simplicity of the method and apparatus allows for both application in field conditions and acts

as a low cost supplement to actual determinations of uniaxial and compressive strength, which are both costly and relatively time consuming to perform.

No principal stresses are associated with point load tests.

During point load testing a *Maetest Model A125* was used. It is equipped with two differently scaled needle gauges showing the applied force, in which drag needles indicate the maximum applied force with an accuracy of 0.2 kN in the smaller scale and 2 kN in the larger. The maximum force readable in the smaller scale is 5.6 kN and the maximum value on the larger scale is 56 kN. Specimens tested stronger than this value of 56 kN are assigned this maximum.

The time of latest calibration did not appear on the device, and neither did the author calibrate it as recommended in the *ISRM Suggested Method for Determining Point Load Strength*.

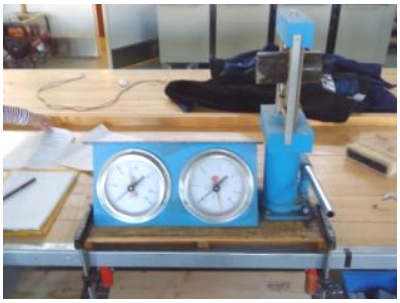

Figure 22: The Maetest Model A125.

4.1.6 Brazilian indirect tensile strength

Tests were performed following the *ISRM Suggested Methods for Determining the Tensile Strength of Rock Materials* (1978), to which detailed descriptions are referred to. The Brazilian test yields the indirect tensile strength of a cylindrical specimen by applying an increasing compressive force along two diametrically opposite lines of a cylindrical specimen until failure of the specimen. The failure is recommended to take place within 15-30 s after initial loading. The indirect tensile strength σ_t [MPa] is given by the expression

$$\sigma_t = \frac{2 \cdot P}{\pi \cdot h \cdot d} \qquad \textbf{eq. 35}$$

Where P [N] is the applied force at failure. The diameter d [mm] of the specimen should be approximately 2.5-3 times the specimen height or thickness h [mm].

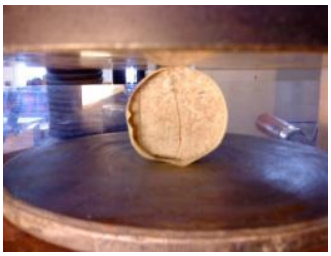

Figure 23: Specimen failure in Brazilian indirect tension.

As seen on Figure 23 the loading platens used were not curved as recommended, but planar.

Specimens were covered with two layers of masking tape along the periphery of the cylinder to ensure that the compressive force distributes evenly along the contact line between specimen and load platens. During the Brazilian tests only the applied force at failure was measured. Strain gauges were not used to *identify* the point of failure. No elastic moduli can be derived from or associated with Brazilian testing. The optimal mode of failure is surface coincident with and parallel to the contact lines, and the failure is primarily tensile, though with smaller compression zones near the contact lines.

The principal stresses, all in [MPa], at failure in Brazilian tests are

$$\sigma_1 = 3 \cdot \sigma_t \wedge \sigma_2 = 0 \wedge \sigma_3 = -\sigma_t \qquad \textbf{eq. 36}$$

These stresses will are handled in greater detail in enclosure 9, where methods of calculating failure envelopes are presented, based partly on the indirect tensile strength, and partly on the unconfined compressive strength.

4.1.7 Unconfined uniaxial compression

Unconfined uniaxial compression tests were carried out following the *ISRM Suggested Method for Determining the Complete Stress-Strain Curve for Intact Rock in Uniaxial Compression*. The aim of the tests was for each of the tested specimens to determine the unconfined compressive strength σ_c and static Young's modulus E_{stat} via constructing partial, not complete, stress-strain curves.

Test specimens are recommended to tave a height-diameter ratio of 2-3, and are not to be significantly smaller than Ø 50 mm. The tested specimens were all cylindrical, except for the two F-series specimens, which were not cored, but prepared with the rock saw in to specimens in the shape of rectangular prisms, with desired dimensions of 50mm·50mm·100mm.

For a specimen of initial crossectional area A_0 [mm^2] perpendicular to the loading direction, the unconfined compressive strength is given as

$$\sigma_c = \frac{P}{A_0} \qquad \textbf{eq. 37}$$

Where P is the applied force at failure.

The axial strain ε_a [-] is given by

$$\varepsilon_a = \frac{\Delta h}{h_0} \qquad \textbf{eq. 38}$$

Where Δh [mm] is the change in height, and h_0 [mm] is the initial height of the specimen. Strains in hard rock are often best represented as parts per thousands, i.e. [‰].The calculated strains are negative, since Δh becomes negative in compression, but the usual convention in rock mechanics is to assume compressive effects are positive.

If diametric strain gauges were utilized, the diametric strain would be given by

$$\varepsilon_d = \frac{\Delta d}{d_0} \quad \text{eq. 39}$$

Where Δd [mm] is the change in diameter, and d_0 [mm] is the initial diameter of the specimen. The diametric strain is equal to the circumferential strain. Further would the calculation of static Poisson's ratio be facilitated if diametric strains were measured. The static Poisson's modulus ν_{stat} [-] is given by

$$\nu_{stat} = -\frac{d\varepsilon_d}{d\varepsilon_a} \quad \text{eq. 40}$$

Poisson's ratio is of great relevance to evaluate, since it is related to the rock stress coefficient at rest K_0 [-], which is also defined as the ratio of the minor principal stress to the major principal stress. The coefficient is given by

$$K_0 = \frac{\sigma_3}{\sigma_1} = \frac{\nu}{1-\nu} \quad \text{eq. 41}$$

Together with the density ρ [kg/m^3] and depth below surface z [m], the major and minor principal stresses can be evaluated as

$$\sigma_1 = \rho \cdot g \cdot z = \gamma \cdot z \quad \text{eq. 42}$$

$$\sigma_3 = K_0 \cdot \sigma_1 = K_0 \cdot \gamma \cdot z \quad \text{eq. 43}$$

Where g [m/s^2] is acceleration of gravity.

The static Young's modulus E_{stat} is given by

$$E_{stat} = \frac{d\sigma_1}{d\varepsilon_a} \quad \text{eq. 44}$$

When inserting σ_1 in [MPa] and ε_a in [‰], E_{stat} is evaluated in [GPa]. The static modulus is preferebly evaluated at a stress level of 50 % of that of the unconfined compressive strength, on a *loading* branch, not unloading. In practice the infinitesimal expression is evaluated as a least squares linear fit centered at the 50 % stress level.

The evaluation of the static modulus provide means of comparing it with determined dynamic moduli.

Before beginning actual testing some specimen specific planning must be considered, since the strain gauge cannot be installed all the way through to failure, because of risk of breaking the gauge for later use. To facilitate the planning, it is of importance, that either Brazilian or point load tests from the same specimen series are carried out in advance, since these provide means of empirically evaluating the unconfined compressive strength. According to Foged (2009) the unconfined compressive strength is roughly 8-12 times the numerical value of the indirect tensile strength, and according to *ISRM Suggested Method* on the subject, the unconfined compressive strength is roughly 20-25 times the point load index. These strength estimates in [MPa] are then converted to units of force [N] by multiplying them with the crosssectional area [mm^2] of the specimen to be tested, yielding an expected maximally applicable force to the specimen. Here it is convenient to use the units mega Pascal [MPa] and square millimetres [mm^2] since the product of these are in Newton [N]. During testing

with the strain gauge installed, i.e. before failure, the maximal force to be applied is chosen to be approximately 0.7 times the estimated applied force at failure.

The principal stresses in [MPa] at failure in unconfined compression tests are given by

$$\sigma_1 = \sigma_c \wedge \sigma_2 = 0 \wedge \sigma_3 = 0 \qquad \textbf{eq. 45}$$

These will be handled in greater detail in enclosure 9, where methods of calculating failure envelopes are presented, based partly in the unconfined compressive strength, and partly the indirect tensile strength.

Uniaxial compression tests and Brazilian tests were carried out using a *Seidner Form Test 101/1200 ED* hydraulic test machine, and was originally purposed for concrete testing of larger concrete specimens. To accommodate the smaller rock specimens considered in this report, it was necessary to place metal plates between the load platens of the device, since the hydraulic pistons only has a restricted range of movement. The upper load plates is seated in a ball bedding, enabling the platen to rotate and tilt during loading and there reduces the effect from specimen ends being non-parallel, *ISRM Suggested Method for Determining the Complete Stress-Strain Curve for Intact Rock in Uniaxial Compression (1998)*. Further were circles drawn onto the upper loading platen, securing that all specimen centers aligned with the center of the spherical joint, which made the upper platen tiltable.

Figure 24: Test setup for unconfined compressive tests.

The machine delivers a maximal compressive force of 1200 kN, and a digital read-out display gives the applied force to within 0.1 kN. When running a specimen to failure a *peak*-button is pushed down, which dictates the maximal compressive force yet applied to be displayed. The applied force and its rate of application are controlled *manually* by turning a valve which pressurizes the oil in the hydraulic pistons. A separate valve is used to decompress the hydraulic pistons, and is sufficiently sensitive to facilitate conductance of controlled unloading sequences. Since the loading and unloading sequences are controlled manually, the conducted tests will not be standardized with respect to loading and unloading rates, since the operating quality depends on the testing personnel's experience with the machine. Further does manual control exclude the possibility of declaring a *control variable*, such as the commonly used axial displacement. The used strain gauge, *Tesa Digico 10 type 019.30100*, works by being fixed magnetically at its base to the inserted metal plates, and deformations push down a vertically positioned rod, which is connected to the actual measuring instance in the gauge. The

used strain gauge has a resolution of 1 µm. All data were written down by hand, and later typed in to a computer.

The strain gauge was installed to measure between the upper loading platen and the larger reddish metal plates in the loading train, thus including measurement of strains in the smaller metallic plates as seen in Figure 24 and Figure 25.

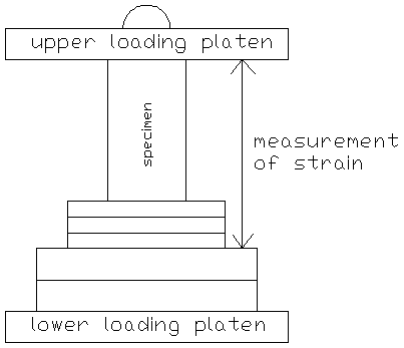

Figure 25: Strain measurement.

The strain gauge could not be installed differently and more optimal, because of the impractical dimensions of the gauge itself. A sequence of loading and unloading paths were run through depending on the specimen properties and dimensions. These loading sequences facilitates the calculation of Young's modulus. Finally, after removing the strain gauge from the setup, the specimen is brought to failure within the recommended time window.

Figure 26: Strain gauge.

Maintenance figures on the hydraulic test machine did not clearly state when the latest calibration took place, and neither did the author attempt to calibrate it.

To fulfil safety requirements, the test machine was equipped with plexiglass to prevent violent failures to hit the testing personnel with flying fragments. Further did the testing personnel wear safety glasses and ear plugs during testing.

4.2 Tested specimens

Laboratory work was carried out on specimens of 6 petrographically different igneous and metamorphic rock types. These 6 specimen series are referred to as specimen series A through to F included. The specimen rock types are listed in Table 12. Further can specimen data sheets be seen in enclosure 10, these contain dimensions, density calculations, p-wave velocities, dynamic and static Young's modulus, failure data, other remarks and pictures after compressive testing.

Table 12: Considered petrological rock types.

A	GRANODIORITE
B	monzonitic GNEISS
C	CHARNOCKITE of granitic texture and fabric
D	GRANITE
E	granulite facies GNEISS
F	biotitic augen GNEISS

Table 13: Specimen series and number of performed tests.

specimen	bulk density	p-wave velocity	Brazilian test	point load test	unconfined compression
series A	6	6	3	6	3
series B	6	6	3	5	3
series C	6	6	3	5	3
series D	3	2	1	11	2
series E	3	2	1	11	2
F-0	1	2	0	6	0
F-30	1	1	0	3	0
F-60	1	2	0	11	0
F-90	1	1	0	3	0
F-pt	2	2	0	8	2

The specimens A through to E were cored specimens were and stored in an unheated outdoor shack at the Building & Construction School in Sisimiut. The dates of the borings and sampling depths were not clearly specified on the core boxes, but this information is luckily not of large relevance for the laboratory work sessions and the subsequent data analysis, and would only have served a formal purpose when presenting the specimens. Specimens in the F series was sampled during the field investigations at the Tasersuaq hydropower project site, at the access/maintenance tunnel and at the pressure tunnel. The positions of station 0 m and 100 m and the pressure tunnel site can be seen in enclosure 2. This F series is further divided into F-0, F-30, F-60, F-90 and finally F-pt, where the numbers refer to the station (from the start of the access tunnel) at which the sample was taken, and '*pt*' refers to the sample was taken from the pressure tunnel.

A series of tests and measurements were intended to be carried out on each specimen series. These tests and measurements include the following: petrographical description, determination of bulk density, measurement

of p-wave velocity, Brazilian indirect tensile strength test, point load strength, unconfined compression test to determine the unconfined compressive strength and the static Young's modulus. The Table 13 shows which tests and the number of tested specimens. All specimens were kept in damp cloths until the point of testing.

5 Findings and results

In the following the obtained results will be presented. First the field investigations, then followed by the laboratory work. This also follows the natural succession in the analysis flow.

5.1 Refraction seismic

To examplify the procedure when performing the velocity analysis of the refractor, the single spread performed at the pressure tunnel is utilized. Picked data from this spread is seen in Table 14.

Table 14: Refraction seismic data from the pressure tunnel site.

offset [m]	forward travel times [µs]	reverse travel times [µs]	t^- [µs]	$v_{p,AB}$ [km/s]	v_p [km/s]	r^2 [-]
0	0	2290	-2290	3,20	2,86	0,9935
2	600	1640	-1040	3,15		
4	1100	870	230	2,33		
6	1950	0	1950	-		

Here $v_{p,AB}$ given in column 5 are values based on only the slopes between two adjacent t^- terms (between 1 and 2, 2 and 3, 3 and 4), and the single v_p given in column 6 is calculated by the slope of the entire t^- term curve. The coefficient of determination r^2 [-] is calculated for the linear correlation between t^- and offset, as seen in Figure 27.

The different velocities are shown in Figure 27, as are the travel times and t^- terms are plotted. The velocities are showed as constant values in the considered offset intervals of the corresponding geophone placements, but could alternatively be represented as a single velocity representative in the geometrical centre of the considered interval.

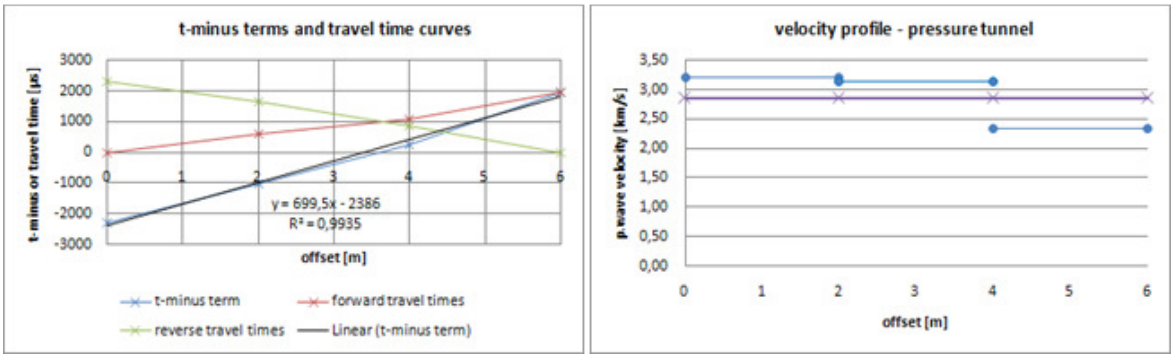

Figure 27: Travel time curves and velocity profile from the pressure tunnel site.

The velocities in Figure 27 and in Table 14 yields a velocity along the spread as a whole of 2.86 km/s.

As a curious note, the author has found that the harmonic mean of the velocities found by linear regression on the forward and reverse travel time curves from the refractor, yield the numerically same result, as when calculating the refractor p-wave velocity by performing least squares linear regression on the t^- terms over the entire spread. The author could not find this stated in the literature.

For the data from the access/maintenance tunnel overdeterminations were measured, because of the overlap. The complete data set is seen in enclosure 11, were cells of the same colour correspond to values belong to the same spread. The data sheet contains 16 columns, which will be presented here below, where numbering identify each column.

1: Contains the stationing along which the profile extends. A lower valued station corresponds to it being closer to the tunnel entrance in the bedrock.

2 & 3: Indicates the spread number and its position along the stationing, including overlaps.

4+5: Contains the *forward* travel times for each spread along the profile. Notice that overlaps of the forward travel times are indicated.

6+7: Contains the *reverse* travel times for each spread along the profile. Notice that overlaps of the reverse travel times are indicated.

8+9: Contains the averaged *forward* travel times, where averaging is performed for overdetermined forward travel times. Overlapping spreads are still indicated.

10+11: Contains the averaged *reverse* travel times, where averaging is performed for overdetermined reverse travel times. Overlapping spreads are still indicated.

12+13: Contains the t^- term of each spread, where $t^- = t_{nF} - t_{nR}$ [µs]. The values are calculated from the averaged travel times. Overlaps are still indicated.

14: Contains the p-wave velocity calculated as $v_p = 2/m(t^-)$ [km/s], where m(t-) [ms/m] is the slope of the linear *t^- versus offset plot* where all 4 first arrivals are included. These velocities are calculated for each spread, and the calculated velocity is representative in the geometric centre of the spread, or as a constant value over the entire spread.

15: Contains the moving average of two velocities of two adjecent/overlapping spreads.

16: Contains the coefficient of determination r^2 [-] between the linear *t^- versus **double** offset* plot, used to determine the refractor velocities. All r^2-values are larger than 0.995.

The Figure 28 shows the obtained p-wave velocity profile from the refraction seismic investigation along the access/maintenance tunnel. The blue curve represent a moving average of the originally obtained velocities for each spread. This moving average is performed to make the data more comparable with the mapped RQD and GSI values, which were evaluated for 10 m sections during excavation, which make up a lower data density than the original seismic data.

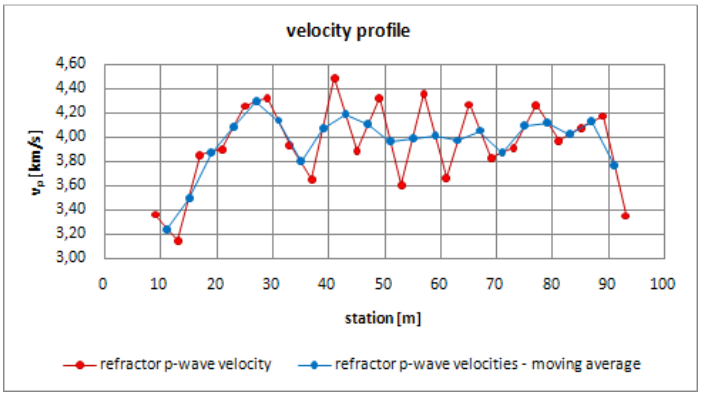

Figure 28: Velocity profile along the access/maintenance tunnel.

As seen on the profile in velocity profile, the velocity increases with 1.06 km/s from 3.23 km/s at station 11 m to 4.29 km/s at station 27 m. From station 39 m to 87 m, the velocity is almost constant around 3.9-4.2 km/s, the average is 4.05 km/s. At station 91 m the velocity takes on the value 3.76 km/s, which is lower by 0.29 km/s relative to the average velocity encountered from station 37 m to 87 m.

5.2 Schmidt rebounds

The complete data from Schmidt rebound measurements are seen in enclosure 12. From these data sheets the the mean values from the access/maintenance tunnel are plotted versus stationing in Figure 29. The used data series are the ones where impacts are separated, not coincident.

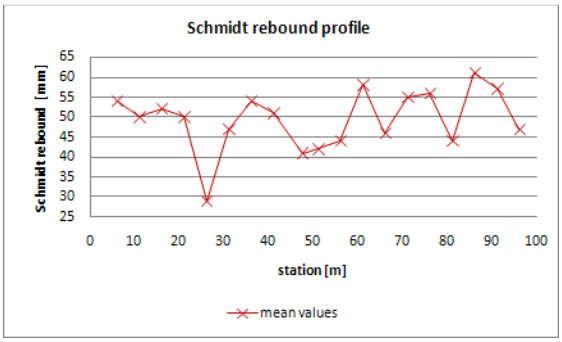

Figure 29: Schmidt rebound profile.

Relative degrees of weathering can be obtained from Schmidt rebound profiling on the same rock type, since lower rebounds indicate higher degree of weathering. This fact is hard to apply on the profile in Figure 29, since shotcrete droplets were observed on almost all surfaces, making rebounds questionable, since the shotcrete alters the rebound values. Further does the *ISRM Suggested Method* state that the *de*crease in rebound between the first two coincidental impacts can be used as a mechanical index of weathering, but all but one measurement series did show an *in*crease from the first to the second coincident impact, hence being opposite than expected.

The means in Figure 29 range from R_N=29 mm to R_N = 61 mm, which corresponds to R_L = 21 mm and R_L = 51 mm. These extreme values yield compressive strengths between σ_c = 6.42 MPa and σ_c = 52.7 MPa, respectively, when inserted into correlation in eq. 26. But the scattered droplets of shotcrete should again be taken into account, since the presence of these produce smaller rebounds. The average Schmidt rebound along the access/maintenance tunnel is R_N = 49 mm, or R_L = 40 mm, which corresponds to σ_c = 24.5 MPa when inserted into eq. 26.

Mean Schmidt rebounds from the pressure tunnel site are listed in Table 15. These were measured with the Schmidt hammer pointing 36 degrees downwards.

Table 15: Schmidt rebounds from the pressure tunnel site.

	coincident [mm]	coincident L-type [mm]	separated [mm]	separated L-type [mm]	coincident corrected [mm]	separated corrected [mm]
mean	60	50	51	42	51	43
median	61	51	50	41	52	42
mode	62	52	54	45	54	46
max.	64	54	61	51	56	52
min.	49	40	39	31	42	32
range	15	14	22	21	14	20

The interesting figures in Table 15 are the direction corrected and from N-type to L-type converted values in the two last columns. The *separated* values are used in in further analysis, as recommended in the *ISRM Suggested Method* on the subject.

An estimate of the unconfined compressive strength σ_c [MPa] can be calculated on the basis of the mean rebound value of the separated impacts. The correlation is given by eq. 26.

Using the value R_L = 43 yields σ_c = 29.4 MPa.

5.3 Engineering geological mapping

A multitude of parameters were mapped in the tunnels. The mapping data can be seen in enclosure 13. The mapped features will be presented in general overview in the following.

5.3.1 Access/maintenance tunnel

Since the roof of the tunnel had been sprayed with stabilizing shotcrete, and the floor was covered with fill, only the walls were amenable for mapping. This also made it difficult to identify joints (nearly) parallel to the tunnel trace direction. So in general only joints dipping weakly (with spacings smaller than the tunnel dimensions) and joints almost perpendicular to the tunnel were identified. Some intermittent joints were though seen, to assemble the normally encountered three subparallel joint sets.

The rock type observed thruoghout the access/maintenance tunnel *moderately hard, biotitic augen GNEISS, red and dark grey, medium to very coarse grained (microcline, biotite mica), very weakly foliated (weakly lenticular microcline crystals).*

For the access/maintenance tunnel the general joint spacings were moderately close to very wide, where only few moderately close joint were observed.

The most frequently observed joint striked in average 260 degrees and were dipping steeply. Not many consistent joint dips below 20 degrees were observed, due to what is meant to be very wide spacing.

Persistances of these joints were in general restricted by the tunnel extents (appr. 5 m) and some discontinued in the rock mass, though was one weakly dipping joint near station 90 m showing persistance in excess of 20 m.

Seepages were minimal, since water flow was minimized by the below freezing temperatures, despite of this few ice formations were seen as an indication of water flow into the tunnel.

No filling material was encountered in joints, which in general were tight, i.e. having no aperture.

Weathering of the tunnel walls was only encountered as slight weathering near the tunnel entrance and elsewhere the rock was fresh. Joint walls were in some cases moderately weathered, especially near the tunnel entrance, but in general fresh to slightly weathered.

Hardnesses near the tunnel entrance were of degree R3, whilst it was R4 for the remaining parts of tunnel.

No slickensided joints were observed, only few slightly rough planar joints were observed. The JRC_0 value of Barton was at minimum 4-6, but in general about 8. Wavinesses were at minimum estimated to be 0.05 m per one meter, and in general of the magitude 0.05-0.1 m per one meter.

The observations of the GSI are plotted in Figure 30 with the RQD mappings of Istak.

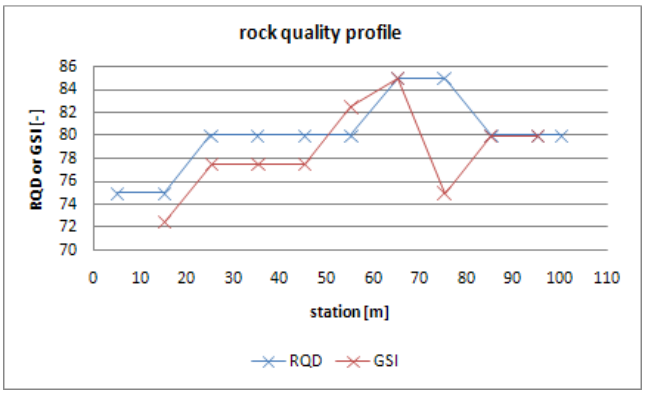

Figure 30: Rock quality profile from tunnel mapping.

The GSI estimates are all within the range from 72.5 (average of 70 and 75) to 85, corresponding to massive good quality rock, and the mapped RQD values are all within the range from 75 to 85, corresponding to good quality after *Deere (1967)*. The two different classification schemes exhibit general trends, which are very comparable, i.e. increasing near the entrance (station 0 m to 25), followed by a constant plateau (from station 25 m to appr. 50 m), followed by an increase at station 70 m, and they both decrease at station 75 m.

No shear zones of very blocky or disturbed rock was observed, and joints did not show tendencies of being fatally unstable, since no slickensides or infill was observed, and spacings were large. But important features parallel to the tunnel could not be mapped as desired due to the shotcreted roof. The mapped features and GSI and RQD values all support the statement that the considered bedrock in the access/maintenance tunnel in general is *competent*.

5.3.2 Pressure tunnel site

The pressure tunnel site, included in this report is located near a zone where tunnel collapse occurred. Also here the roof was shotcreted.

The same rock type as in the access/maintenance tunnel was observed.

Here one very dominant joint is observed. The dip is nearly vertical, at 85 degrees, and joints are closely spaced. Intermittent joints discontinued by the dominant set were observed randomly.

The dominant joints persist further than the tunnel extent, being 5 m.

Joint apertures are tight, but the degree of seepage is larger than seen in the access/maintemance tunnel, probably since the temperature is above freezing at this position deeper in the tunnel system. The observed seepages are of category II to III, with occasional drops.

Joint walls were weathered moderately.

The joint roughnesses were rough planar, with JRC_0 values of 8-10, and the waviness was estimated to be 0.1 m per one meter.

The estimated GSI is 45-50 corresponding to *very blocky fair quality*, and the mapped RQD value is 40 (by Istak), corresponding to *poor* quality, after *Deere et al. (1967)*.

The rock mass at this site possess poor to fair quality, and *cannot* be termed competent.

5.4 Intact rock descriptions

The the petrological intact rock descriptions of the rock types considered in this report are seen in Table 16.

Table 16: Intact rock descriptions.

specimen series A	hard to very hard, fresh GRANODIORITE, dark grey, medium grained (hypersthene/hornblende, quartz), equigranular, isotropic.
specimen series B	hard, monzonitic GNEISS, light to dark grey (predominantly light grey), medium to coarse grained (both plagioclase and orthoclase feldspars, minor ammounts of hornblende), weakly foliated 80° w.r.t. longtitudinal axis
specimen series C	moderately hard, fresh CHARNOCKITE of granitic texture and fabric, primarily light grey with greenish iridescens, medium to coarse grained (quartz, perthite, hypersthene), isotropic
specimen series D	hard to very hard, fresh GRANITE, pink, medium-coarse grained (microcline, quartz), isotropic though transitioning irregularily between medium and coarse grained crystallizations
specimen series E	moderately hard, fresh granulite facies GNEISS, grey, coarse grained (quartz, plagioclase feldspars, hornblende), weakly foliated
specimen series F	moderately hard, fresh to slightly weathered biotitic augen GNEISS, red and dark grey, medium to very coarse grained (biotite mica, microcline) very weakly foliated (lenticular, very coarse microcline crystals)

5.5 Determined bulk densities

The found densities of the rock types considered in this report are seen in Table 17.

Table 17: Determined bulk densities.

specimen series	# of measurements	ρ [g/cm^3]	standard deviation [g/cm^3]
A	6	3,03	0,04
B	6	2,79	0,07
C	6	2,65	0,02
D	3	2,61	0,01
E	3	2,80	0,01
F	4	2,85	0,01
F-pt	2	2,81	0,004

In the table the specimen series F refers to specimens taken from the access/maintenance tunnel, and F-pt refers to specimen sampled from the pressure tunnel site. The entire F-series volumes were determined by means of buoyancy, and a single Brazilian test specimen from series C, D and E were also determined in the same manner. The remaining volumes were determined geometrically.

The bulk densities range from 2.61 g/cm^3 for specimen series D to 3.03 g/cm^3 for specimen series A.

5.6 Determined p-wave velocities

Table 18 shows the determined p-wave velocities from the PUNDIT measurements. The given velocities are *length*-weighted averages for each specimen series. The standard deviation of the found average with respect to the individual measurements in the series are also included.

Table 18: determined p-wave velocities.

specimen series	# of measuments	v_p [km/s]	std. deviation [km/s]
A	6	6,24	0,189
B	6	5,73	0,078
C	6	5,68	0,369
D	2	4,28	0,094
E	2	4,32	0,186
F-0	2	4,66	0,002
F-30	1	4,52	NA
F-60	2	2,85	0,063
F-90	1	2,64	NA
F-pt	2	3,56	0,180

Velocities range from 6.24 km/s for specimen series A to 2.64 km/s for the sample F-90 from the access/maintenance tunnel. The very low velocities of samples F-60 and F-90 are questionable, and will be discussed later on.

The effects of saturation on the p-wave velocity have been investigated for a two specimens which were tested, one from series E and D each. Velocities were determined in the same manner as the above, but both after evacuation in a water bath for 24 h, and after drying for 24 h at 105 °C. The results are seen in Table 19. The specimens were UCT-D-2 and UCT-E-2, where 'UCT' refers to that the specimens were tested in unconfined compression later on.

Table 19: Effects of water saturation on v_p.

specimen	$m_{saturated}$ [g]	m_{dry} [g]	water content [g]	volume [cm3]	estimated porosity [‰]	saturated V_p [km/s]	dry V_p [km/s]	relative velocity increase
D	440,62	439,45	0,266	169,3	1,57	4,72	**3,62**	**0,30**
E	474,37	473,07	0,275	169,4	1,62	5,22	**3,88**	**0,34**

The saturated weight of the specimens corresponded to a saturated surface condition after evacuation in the water bath, and the dry weights was after 24 h of drying at 105 °C.

The porosity of the specimens was estimated by the relation

$$\varphi = \frac{\left(\frac{m_{water}}{\rho_{water}} \right)}{V_{specimen}} \qquad \text{eq. 46}$$

This is assuming that the entire (open) porevolume is water filled. The estimated porosities are in the parts per thousand range, as expected for hard igneous and metamorphic rocks.

The increase in velocity are, when evaluated relative to the dry state, from 30 to 34 %, which is quite significant.

5.7 Determined point load indices

Table 20 shows the calculated point load indices for each specimen series.

Table 20: Determined point load indices.

specimen series	# tests	arithmetic value [MPa]	graphical value [MPa]	r^2 [-]
A	6	10,4	*9,93*	0,989
B	5	10,5	*10,4*	0,840
C	5	7,72	*7,69*	0,939
D	11	6,6	*5,46*	0,740
E	11	7,77	*7,61*	0,949
F-0	6	3,88	*2,2*	0,943
F-30	3	2,40	-	-
F-60	11	2,68	*2,99*	0,849
F-90	3	2,76	*2,39*	0,966
F-pt	8	2,65	*2,59*	0,691

In the table, both the arithmetic mean of the size corrected, by means of the factor F, are showed, as are the graphically size corrected, with the corresponding coefficient of determination r^2 of the corresponding linear fit.

The full test data can be seen in enclosure 14. In the enclosure the extreme values of $I_{s(50)}$ [MPa] which have not been included in the arithmetic average, as recommended in the relevant *ISRM Suggested Method*, are ~~striked through~~ with a line. For test series with more than or exactly 10 performed and valid test this exclusion is done. Further are the values of $(D_e)^2$ [mm^2] and P_{max} [kN] which *are* included in the linear regression, are typed with **bold underlined** numbers. The data which have been excluded, do not fit the linear relationship well, and can therefore be excluded in the regression analysis, as recommended is the relevant *ISRM Suggested Method.* The linear plots of P_{max} [kN] versus $I_{s(50)}$ [MPa] are not shown in the enclosures, since the graphical method has been reformulated into an analytical problem, which was solved using the *goal seek* and statistical functions in Office Excel.

Data which have been used for further analysis are the graphically size corrected point load indices, since the relevant *ISRM Suggested Method* recommends these data as the most reliable.

In general the graphically size corrected point load indices are larger than the arithmetic means, but there is no significant discrepancy between the data from the two methods, except for series F-0 where the difference is 76 %, relative to the graphical value.

The largest point load index is that of specimen series B, and the smallest is that of specimen series F-0. It could be discussed if A or B yields the greater point load index, since specimen series A has better linear correlation than that of specimen series B, which therefore makes the determination of the graphical value more uncertain for specimen series B.

5.8 Compressive testing data

The entire set of failure data for each specimen, which has either been tested for unconfined compressive strength σ_c [MPa] or for Brazilian indirect tensile strength σ_t [MPa] are shown in Table 21.

Table 21: Results from compressive testing including dynamic elastic moduli.

	σ_c [MPa]	σ_t [MPa]	E_{stat} [GPa]	stress level	E_{dyn} [GPa]
A-1	151,1	9,41	57,7	0,28	122,8
A-2	141,8	10,5	20,5	0,22	117
A-3	161,8	9,88	33,1	0,18	118
mean	**151,6**	**9,95**	**37,1**	-	**119,3**
std. dev.	10,03	0,565	18,9	-	3,101

	σ_c [MPa]	σ_t [MPa]	E_{stat} [GPa]	stress level	E_{dyn} [GPa]
B-1	113,1	9,93	26,2	0,30	89,2
B-2	no failure	11,8	17,8	NA	96,1
B-3	162,0	7,78	34,6	0,20	88,4
mean	**137,5**	**9,84**	**26,2**	-	**91,2**
std. dev.	34,58	2,01	8,40	-	4,234

	σ_c [MPa]	σ_t [MPa]	E_{stat} [GPa]	stress level	E_{dyn} [GPa]
C-1	161,0	7,59	25,3	0,21	81,1
C-2	155,8	7,92	29,6	0,22	79,9
C-3	80,19	8,07	14.6	0,43	79,2
mean	**132,3**	**7,86**	**27,5**	-	**80,1**
std. dev.	45,24	0,250	3,04	-	0,961

	σ_c [MPa]	σ_t [MPa]	E_{stat} [GPa]	stress level	E_{dyn} [GPa]
-	-	-	-	-	-
D-1	217,0		16,7	0,18	49,5
D-2	143,0	10,67	11,3	0,27	45,9
mean	**180,0**	**10,67**	**14,0**	-	**47,7**
std. dev.	52,34	NA	3,82	-	2,546

	σ_c [MPa]	σ_t [MPa]	E_{stat} [GPa]	stress level	E_{dyn} [GPa]
-	-	-	-	-	-
E-1	142,4		10,9	0,28	49,1
E-2	86,9	8,1	13,6	0,45	55,3
mean	**114,6**	**8,09**	**12,3**	-	**52,2**
std. dev.	39,2	NA	1,91	-	4,38

	σ_c [MPa]	σ_t [MPa]	E_{stat} [GPa]	stress level	E_{dyn} [GPa]
-	-	-	-	-	-
F-1	30,1		7,32	0,67	38,3
F-2	38,8	3,24	9,63	0,52	33,3
mean	**34,4**	**3,24**	**8,48**	-	**35,8**
std. dev.	6,2	NA	1,63	-	3,54

The tables further includes the static Young's modulus E_{stat} [GPa], and the dynamic Young's modulus E_{dyn} [GPa]. Further do the tables contain the relative stress level at which the static moduli where evaluated, the reference stress being the unconfined compressive strength.

The obtained stress-strain curves with unloading and loading branches and the corresponding data sheets are seen in enclosure 15.

From the tables it is seen that specimen series D yielded the highest mean unconfined compressive strength σ_c = 180.0 [MPa], and the lowest mean σ_c = 34.4 [MPa] was found for specimen series F. It is further seen that the Brazilian indirect tensile strength σ_t = 10.67 [MPa] for specimen series D is the highest and the minimum is σ_t = 3.24 [MPa] for the synthetic value in the F-series. Notice for the specimens F-1 and F-2 that the evaluated indirect tensile strength is synthetic, and based on the point load index. The specimens F-1 and F-2 are from the pressure tunnel site.

The stress levels at which the static moduli were evaluated ranged from $0.18 \cdot \sigma_c$ [MPa] to $0.67 \cdot \sigma_c$ [MPa].

Table 22 shows different ratios of the means of the found parameters from the compressive testing.

Table 22: Ratios of strenghts and elastic moduli.

specimen series	σ_c/σ_t	E_{stat}/σ_c	E_{dyn}/σ_c	E_{dyn}/E_{dyn}
A	15,2	245	787	3,2
B	14,0	191	663	3,5
C	16,8	207	605	2,9
D	16,9	78	265	3,4
E	14,2	107	455	4,3
F	10,6	246	1040	4,2

The ratio between σ_c and σ_t ranges from 10.6 for specimen series E to 16.9 for specimens series C.

The ratio between the static modulus and the compressive strength ranges from 78 for series D to 245 for series A.

The ratio between the dynamic modulus and the compressive strength ranges from 265 for series D to 1040 for series F.

The more remarkable ratio is the one between the dynamic and static moduli, ranging from 2.9 for series C to 4.3 for series E.

The internal cohesion and the friction angles for each specimen series have been determined as presented in enclosure 16; the shown values in Table 23 are the central estimates of results from each method described in enclosure 9. The entire failure envelope analysis is seen in enclosure 16, these are presented as spread sheets of the failure data in the different representations.

Table 23: Determined friction angles and internal cohesions.

specimen series	A	B	C	D	E	F
friction angle ϕ [degrees]	59,8	58,3	62,2	62,2	59,5	52,7
internal cohesion c_o [MPa]	19,6	18,8	15,8	21,4	15,3	5,7

The poorest specimen series is clearly series F, both regarding cohesive strength and friction angle, noting that series F still incorporates the artificial tensile strength obtained from the point load index. And the most competent is series D, also for both cohesive strength and friction angle.

The obtained friction angles for series A-E are in general high, but hard rock do possess high friction angles. For the specimen series A, B and C it was observed, that the failure surface in fact was comprised of two oppositely pointing cones, which is just after the text books. The ideal Mohr-Coulomb failure surface is such two cones, where the apex angle is 90 degrees minus the friction angle. Estimated angles between horizontal and the failure surface of the tested specimens, see Figure 31 an example, were 70-75 degrees, corresponding to 45 degrees plus half the friction angle. This yields friction angle=2·(75-45)=60 degrees, which corresponds well with the calculated values.

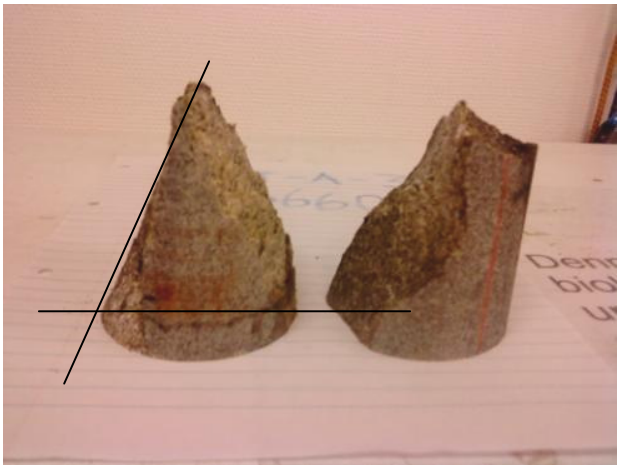

Figure 31: Example of failure surfaces (cones).

The obtained cohesive strengths are high for the series A to E, ranging from 15.3 MPa for series E to 21.4 MPa for series D. The lower value for specimen series F will be discussed later.

Also results obtained from applying the failure criterion of Hoek and Brown via RocLab are shown in Table 24.

Table 24: Obtained results from RocLab computations for intact conditions.

specimen series	m_b [-]	ϕ [°]	c_0 [MPa]
A	11.3	44.3	27.3
B	9.8	42.7	24.8
C	15.7	47.6	24.3
D	15.9	47.8	33.2
E	13.0	32.8	6.2
F	9.1	41.9	7.1

The software has calculated the material parameter m_b [-], noting that s=1 for intact rock, and a corresponding Mohr-Coulomb fit. The HB-criterion evaluates specimen series D to possess the highest value of m_b, and series F to have the lowest. Note that series F still contains the synthetic tensile strength obtained from the point load index.

For the case of intact rock analysis and using the generalized HB-criterion the values GSI=100, D=0, s=1 and a=1/2 are used.

The failure data from each specimen series was separately typed into RocLac, using the '*Use Lab Data*' feature. In the dialog box the minor and major principal stresses for each test are typed in, see Figure 32 for a screen dump of the dialog box.

When applying the laboratory data, the software evaluates intact rock compressive and tensile strength, an estimated deformation modulus E_m [MPa] and the material parameter m_b.

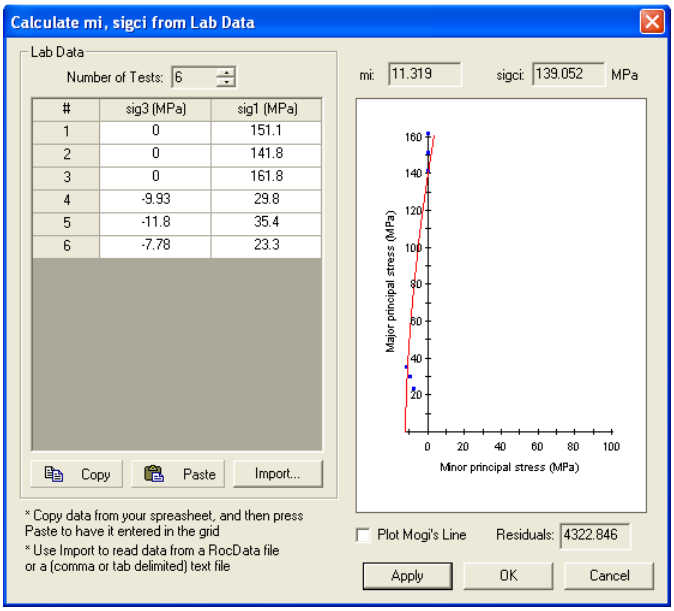

Figure 32: Screendump from RocLab's 'Use Lab Data' feature.

When the data are applied, the program computes the generalized HB-envelope, which easily is exported to Office Excel. An example of the obtained envelopes is shown in Figure 33.

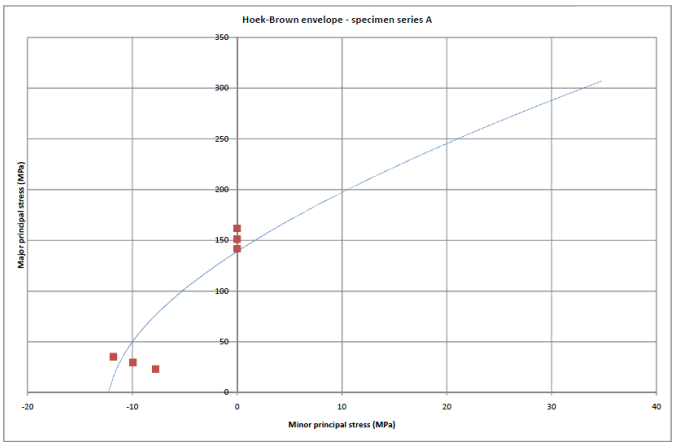

Figure 33: Example of HB-envelope for intact rock.

The envelope for intact rock can be augmented to include mapping data of GSI and evaluation of the disturbance factor D. This is done after typing in the laboratory data, by changing the values of GSI and the disturbance factor D manually.

This is done for the pressure tunnel, whith GSI=50 and D=0.5 for good blasting in jointed, hard rock. The resulting failure envelope is seen in Figure 34.

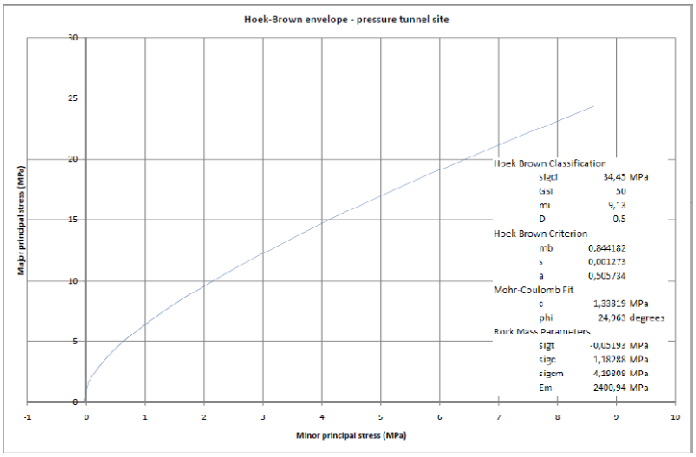

Figure 34: Failure envelope for rock mass at the pressure tunnel site.

RocLab has calculated the parameters a, s, m_b describing the rock mass failure criterion. This is done on the basis of the evaluated GSI, disturbance factor and the laboratory data.

6 Discussion and part conclusions

In the following the results obtained from both field investigations and laboratory measurements will be discussed and compared.

6.1 Refraction seismics

It is of interest to couple the obtained p-wave velocity profiles with the GSI and RQD values from the mapping. First the access/maintenance tunnel is considered.

To correlate the obtained velocities from the 'moving average data' from the refraction seismic to the mapped RQD the correlation in eq. 2 is utilized. The laboratory p-wave velocity is chosen as v_p = 4.6 km/s, which is the average of the F-0 and F-30 laboratory measurements.

The calculated RQD values are shown in Table 25 together with the corresponding velocities.

Table 25: Calculated RQD values from refraction seismic.

station [m]	v_p [km/s]	RQD [-]	station [m]	v_p [km/s]	RQD [-]	station [m]	v_p [km/s]	RQD [-]
11	3,23	49	39	4,07	78	67	4,05	77
15	3,49	58	43	4,18	83	71	3,87	71
19	3,87	71	47	4,10	80	75	4,08	79
23	4,07	78	51	3,96	74	79	4,12	80
27	4,29	87	55	3,98	75	83	4,02	76
31	4,13	81	59	4,01	76	87	4,12	80
35	3,79	68	63	3,97	74	91	3,76	67

The calculated RQD values are plotted together with the mapped RQD and GSI values in Figure 35.

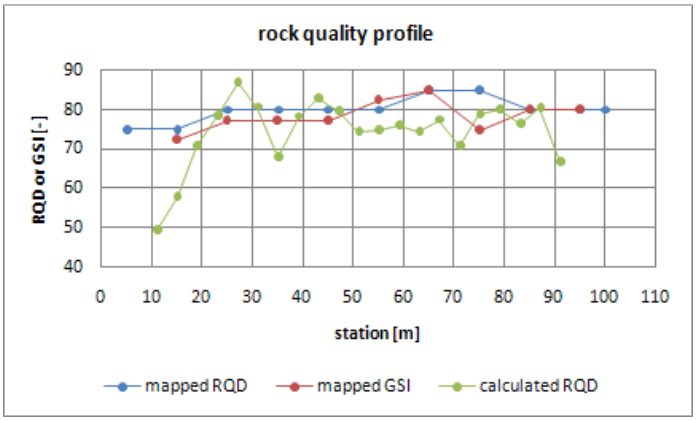

Figure 35: Calculated RQD and mapped rock quality profile.

The calculated and mapped values of the RQD are in general of the same size, which is between 70 to 85. The mean values of the RQD along the entire profile are 74 for the calculated and 80 for the mapped, which show good overall correspondance. Though is there a discrepancy in the lower stationings, where the mapped and calculated RQD values differ from each other significantly. This is interpreted as effects of excavation disturbance, which would not have occurred in undisturbed rock. So no zones of fatal weakness are seen or interpreted from the refraction seismic surveys.

The calculated RQD values are variating more, than the mapped. This is due to both that the mapped values are evaluated from the poorest occurrence along a 10 m tunnel section, and that, more importantly, the p-wave velocity is dependent on many influencing factors, which the RQD and GSI are not, in a direct sense. Further will the p-wave velocity only be effected by joints more or less perpendicular to the direction of propagation, whereas the general evaluation of the RQD and GSI are directionally independent.

The velocities in the velocity profile are increasing until approximately station 25 m. If this is interpreted as the as the station to which weathering effects have reached, the depth of weathering penetration from top of bedrock can be calculated. The tunnel was inclined approximately 45^{o} with respect to the the surface of bedrock, which means the weathering penetration is roughly 25m·cos(45^{o}) ≈ 18 m. This corresponds well with the previous investigations carried out by GTO in 1985, which reported weathering penetrations of approximately 20 m.

The pressure tunnel site yielded p-wave velocities of laboratory based velocity of v_p = 3.56 km/s. Table 26 shows the calculated RQD values between the geophones

The mapped RQD ang GSI was evaluated to be 40 and 45-50, respectively.

Table 26: Calculated RQD values from the pressure tunnel site.

offset [m]	v_p [km/s]	RQD [-]
0-2	3,20	81
2-4	3,15	78
4-6	2,33	43

The velocities between the first three geophones gives high estimates of the RQD, whilst the velocity between geophones 3 and 4 yields a value very comparable with the mapped RQD. This corresponds very well with an observed zone of highly jointed rock at the site, at the same placement as the two considered geophone offsets.

One can evaluate rock mass deformation moduli utilizing the relation in eq. 4 in enclosure 1 from *Barton (2007)*. This is done in Table 27.

Table 27: Rock mass deformation moduli.

offset [m]	v_p [km/s]	Em [Gpa]
0-2	3,20	7,94
2-4	3,15	7,64
4-6	2,33	4,07

The deformation moduli lie between 4 and 8 GPa. The deformation modulus from the RocLab calculations yielded a deformation modulus of 2.4 GPa, as comparison.

6.2 Schmidt rebounds

Schmidt rebounds carried out in the access/maintenance tunnel were obscured by the presence of shotcrete droplets, giving rise to lowered rebound values. The average rebound value for the entire tunnel gave an estimated compressive strength of the encountered rock of σ_c = 24.5 MPa, which is lower than for the pressure tunnel site. This is unlikely the actual value, since the rebound data for the pressure tunnel site yielded larger rebounds and therefore also a higher estimate of the compressive strength of σ_c = 29.4 MPa. The unlikeliness lies in the fact that the rock at the pressure tunnel site was weatered to a larger degree than any of the rock at the access/maintenance tunnel, which should have given rise to lower rebound values.

6.3 Engineering geological mapping

Engineering geological mapping did not include important joint sets near parallel to the tunnels investigated, since the roof of the tunnel were covered with shotcrete.

Nonetheless did the mapping of the access/maintenance tunnel provide sufficient information to conclude that the rock mass was very competent.

The mapping of the pressure tunnel site provided data for the construction of the Hoek-Brown failure envelope of the here considered rock mass, from which rock mass parameters can be *cautiously* estimated.

6.4 Bulk densities

The determined bulk densities all lie in the expected range for rock types encountered in the Sisimiut area. This is based on personal communications with Niels Foged (2009).

The differences of the bulk densities are due the different minerological contents of the considered rock types. Here dark minerals such as amphibole and hypersthene, with recpective densities of 2.9 g/cm^3 and 3.6 g/cm^3, give rise to high densities, as seen for specimen series A. Lower densities occur for rocks containing primarily quartz, orthoclase or plagioclase, with densities ranging from 2.55-2.69 g/cm^3. This is the case for specimens series B through to F.

6.5 p-wave velocities

The determined p-wave velocities for the specimen series A to E all fall in the expected ranges for the considered rock types. From Table 4 the velocities for granite and granodiorite lie between 4.6 and 6 km/s, for gneiss between 3.5 and 7.5 km/s, and the found values ranged from 4.28 to 6.24 km/s, which are contained by the expected velocity range.

The specimens series F from the access/maintenance tunnel, yielded p-wave velocities ranging from 2.64 to 4.66 km/s. The samples from F-60 and F-90 yielded the velocities 2.85 km/s and 2.64 km/s. These are questionable, since field measurements gave rise to a velocity profile along the tunnel, in which all determined velocities are greater than these values. The mean velocity along the field profile is 3.93 km/s. The low velocities for F-60 and

F-90 is interpreted as being effects of the *excavation disturbed zone*, since all specimens were sampled from the tunnel surface, and the samples were those blocks which in fact could be wedged loose from the tunnel wall. The measurements of the intact specimens are not believed to be compromised by misconducted measurements, since 4 measurements of the specimen length was carried out, as were 10 measurements of the travel time conducted. Further was this procedure carried out twice on sample F-60, one on two different specimens.

The sample F-pt, also from the F series but sampled at the pressure tunnel site, yielded a p-wave velocity of 3.56 km/s, which is acceptable, but still outside the range for intact, non-weathered mica gneiss, which spans from 5.5 to 5.8 km/s. So the discrepancy between expected and measured values, approximately 2 km/s, is interpreted as the combination of the effects of the EDZ, slight weathering.

The effects of water saturation on the p-wave velocity are significant, approximately 30-34 % for the specimens UCT-E-2 and UCT-D-2. An attempt to evaluate the effects of saturation and porosity is done here below.

Since hard rock, like gneisses and granite, often have porosities of 1-2 % at absolute highest and matrix p-wave velocities of approximately 6.5 km/s, the time average relation in eq. 9 in enclosure 1 yields a decrease in velocity of 3.8 %, i.e. from 6.5 km/s to 6.25 km/s, when considering the change from zero porosity to an air-filled porosity of 2 %. And the relation further predicts an increase in velocity of only 3.5 ‰ when going from a dry 2%-porosity state to a fully water saturated 2%-porosity state.

So to explain the increase of 30 %, and not the 3.5 ‰ predicted by the time average equation, other effects must be taken into account.

Referring to Figure 5 in enclosure 1, the effects of water saturation are only considerable when the saturation S_w is above 80 %, which is likely not to occur in sparsely jointed rock masses, since rock is considered impermeable, and therefore leaving only the sparse jointing to comprise any hydraulically permeable paths.

To relate the p-wave velocity to density, a plot of v_p versus density shown in Figure 36.

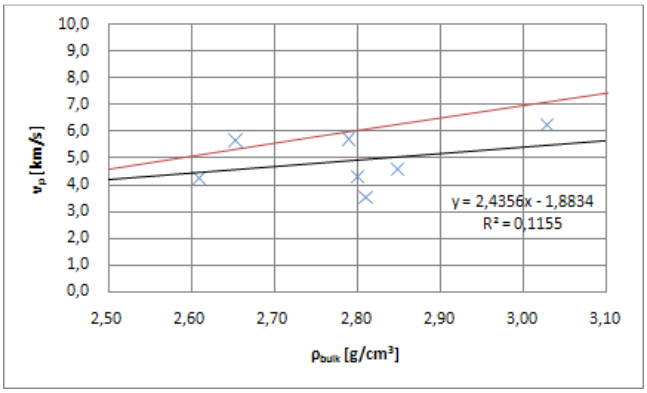

Figure 36: p-wave velocity versus bulk density.

This shows the obtained data, as the blue crosses, and the correlation in eq. 5 enclosure 1, as the linear red curve. The data points are fitted with a linear relation, in black. The linear relations differ significantly, yet should one have in mind the value of the coefficient of determination obtained from the results of this report is only

0.11. The relation in eq. 5 in enclosure 1 is further obtained from a range of petrologically different rocks, making the correlation very general. In general do the relation evaluate higher velocities than actually obtained in relation to this report.

To relate the p-wave velocity to the compressive strength, a plot of σ_c [MPa] versus v_p [km/s] is shown in Figure 37.

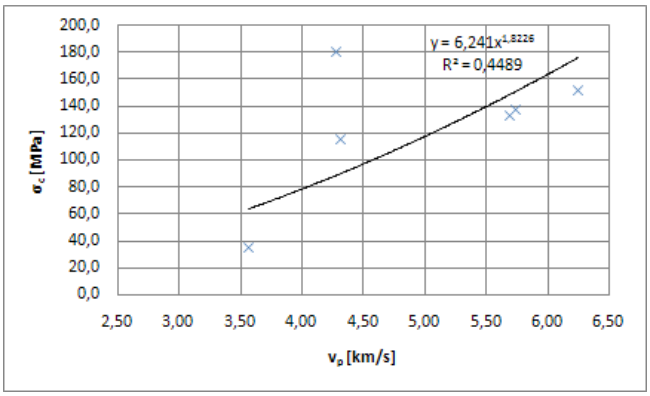

Figure 37: Compressive strength versus v_p.

The data points on the figure are fitted with a power expression, since the literature states a general non-linear expression for the correlation. The expression for the fit only yield an exponent equal to 1.82, as opposed to the general cubical relation stated in the literature.

6.6 Point load testing

Only the point load indices of specimen series D, E and F-60 followed the relevant *ISRM Suggested Method* recommendations of performing at least 10 tests per specimen series. This should taken into when using the data for comparison with other. The *ISRM Suggested Method* states that the unconfined compressive strength is 20-25 times the point load index, and the indirect tensile strength is 1.25 times the point load index.

Table 28: Compressive and tensile stength relative to point load index.

specimen series	$\sigma_c/I_{s(50)}$	$\sigma_t/I_{s(50)}$
A	15,3	1,00
B	13,2	0,95
C	17,2	1,02
D	33,0	1,95
E	15,1	1,06
F	13,3	1,25

It is seen that σ_c is 13.2 to 33 times $I_{s(50)}$, and that σ_t is 0.95 to 1.95 times $I_{s(50)}$. Both ratios differ from the proposed correlations in the relevant *ISRM Suggested Method*, but again should consideration be put into the number of test each parameter are derived from. For example do the indirect tensile strenghts of series D and E

only come from one single test, which make the results very uncertain. But the *ISRM Suggested Method* does inform that the unconfined compressive strength can rabge beween 15 and 50 times the point load index, which thereby included the found ratios.

The ratio $\sigma_t/I_{s(50)}$ is exactly 1.25 for the F series because the indirect tensile strength is calculated from the relation in the *ISRM Suggested Method*.

The point load indices do not show any anisotropical properties in any of the considered rock types.

6.7 Compressive testing

The results obtained included failure stresses of 25 specimens in total and determination of elastic moduli for 16 specimen. These data were combined to calculate the failure envelopes of the 6 petrologically different rock types.

All specimens were tested using the same test setup. This setup included, for the 16 specimens tested in unconfined compression, measurement of strains which included metallic plates, which supported specimens at their lower ends. So the determined moduli corresponded to a length average of that of the specimen itself and the included metal plates, but since all tests were conducted using this setup, the moduli are comparable in a relative sense, but not absolute. The metal plates were also responsible for the large degree of hysteresis seen between loading and unloading branches on the stress-strain curve. A good example of this is the stress-strain curve for specimen, which is seen in Figure 38.

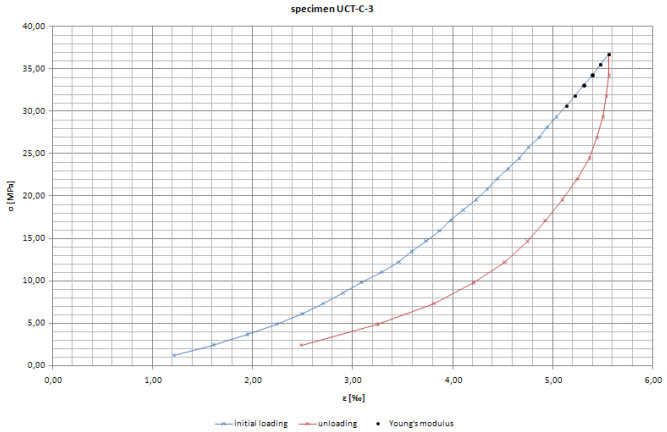

Figure 38: Hysteresis for loading-unloading branches - specimen C-3.

The blue line corresponds to loading and the red to unloading. Notice that the stress-strain curve initially is curving, which can be interpreted as bedding adaptation, including tilting of the upper loading platen. After this curvature the loading branch becomes linear, and the Young's modulus is evaluated from the upper, most linear part of the loading branch, indicated by the black data markers. At a given stress level the loading stops, and an unloading branch is begun measured. Notice that the unloading branch is nearly vertical between the two data markers at the highest stress levels. This yields very large Young's modulus. But the hysteresis is interpreted as only the metal plates are recovering strains when the stresses are relieved, and not as the specimens having very large stiffnesses.

The failure stresses are not effected by the inserted metal plates.

The static versus dynamic moduli are plotted in Figure 39.

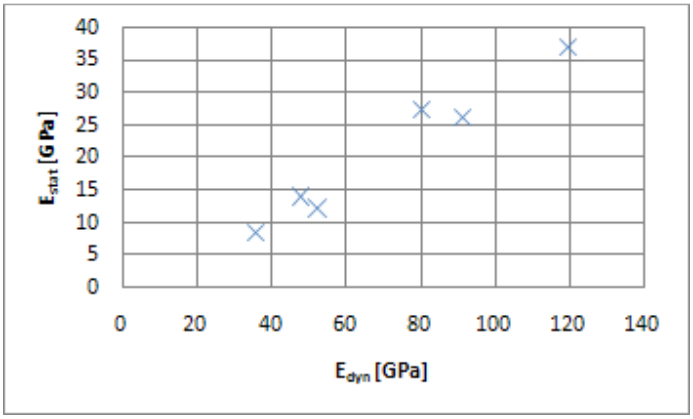

Figure 39: Correlation of dynamic moduli versus static moduli.

An in general increasing trend is seen between dynamical moduli and static moduli, which is also the same trend as the literature states.

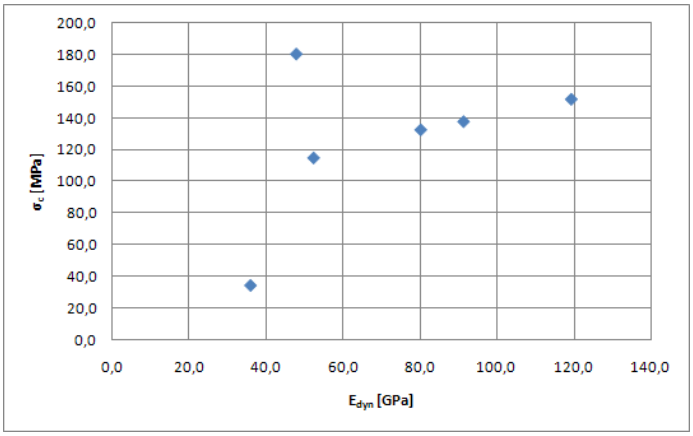

Figure 40: Compressive strength versus dynamic modulus.

Figure 40 shows obtained compressive strengths versus dynamic moduli. The trend is in general increasing, if the veri large compressive strength of specimen series D is not taken into account. No attempts to fit the data points have been made, since no such can be stated in the literature.

The envelopes of specimens A through E included synthetic indirect tensile strengths, which were produced from the corresponding point load indices. These indirect tensile strengths were not included in the failure envelope calculations, but acted as a mean of estimating the quality of the synthetic indirect tensile strength. It is seen from failure envelopes, that the error from using the synthetic indirect tensile strengths are minimal. This implies that the envelopes calculated for specimen series F are valid to a certain degree, since they include the synthetic data in the actual envelope calculations.

During the unconfined compressive tests, the specimen from series A to E failed in a violent, very brittle manner, which defined the point of failure very well. The failures were so violent that specimen B-1 was not brought to failure, because of the endplanes were very non-parallel, which produce fragments shooting sideways at failure. An incident seen at other failures, where the end planes were non-parallel to a lesser degree. The violent failures together with the with the large strength parameters, including indirect tensile strength, compressive strength, friction angle and internal cohesion, indicates that the considered rock types were *very competent*.

The two specimens from the pressure tunnel site behaved differently. Firstly did the specimens not fail as violently as specimens from series A to E. One could see how the specimens started to fail, which formed near vertical tensile failure surfaces. The failure seemed very *ductile*, and the specimens could be taken apart afterwards, since they did not fragment at failure. These circumstances are due to the high content of biotite mica, which is a mineral very susceptible to basal cleavage in one primary plane. Inspection of the failure surfaces provided visual confirmation of the mica content as glittering mica flakes. This mineral is suspected for being the main reason why the F series in general yielded poorer strength parameters than the remaining 5 series.

The envelope calculated for the rock mass, using the Hoek-Brown criterion, at the pressure tunnel site includes the observations of GSI and take into account the effects of blasting by incorporating the disturbance factor D. The envelope shows considerable decrease in strength parameters, which is seen in Table 29.

Table 29: Intact rock parameters versus rock mass parameters - specimen series F.

	INTACT	ROCK MASS
σ_c [MPa]	34,45	4,198
σ_t [MPa]	-3,77	-0,05
GSI [-]	100	50
m_i [-]	9,13	9,13
D [-]	0	0,5
m_b [-]	9,13	0,844182
s [-]	1	0,001273
a [-]	0,5	0,505734
E_m [MPa]	90659,3	2400,94

The rock mass has a compressive strength of roughly one seventh that of the intact rock, and has no significant tensile strength and the deformation modulus has decreased from about 90 GPa to 2.4 GPa. The material parameter m_b is evaluated very low for all specimen series.

Evaluation of the in situ stresses can be achieved by numerical modeling, for example in the finite element code implemented in Plaxis (see www.plaxis.nl for more information on the software). From here stresses can be evaluated by knowing the depth and geometry of the tunnel, with further input such as deformation moduli and densities. This allows for using the found failure criterion for the pressure tunnel, since maximal stresses from the software can be evaluated to see if failure occurs by using the failure criterion. Simple hand calculations

using eq. 41 and eq. 42 are not sufficient, since these do not take into account the effects of stress arching, which occurs in underground excavations

7 Final conclusions

The primary aim of present report is to couple sonic velocities to rock mass properties and quality, where the rock mass consists of hard metamorphic and igneous rock. This is achieved by a combination of field investigations and laboratory measurements.

The previously conducted field investigations utilized in this report is a combination of borings, refraction seismic, engineering geological mapping. Investigations relevant to present report were conducted at the outlet area, nearest to the bottom of the fiord Kangerluarsuk Ungalleq, since this is the investigated area of present report. Field investigations conducted in relation to present report included a refraction seismic profile at the access/maintenance tunnel, and a single spread at the pressure tunnel site, Schmidt hammer rebound measurements, and engineering geological mapping at the two sites. Laboratory measurements on intact specimens included determination of bulk densities, p-wave velocity and associated dynamic moduli, point load indices, compressive and tensile strengths, static Young's moduli, which have been analyzed to reveal possible correlations between parameters obtainable by field methods and parameters obtainable under laboratory conditions.

The findings of investigations in carried out in relation to present report are presented and compared with previous findings in the following.

Determined bulk densities ranged from 2.61 g/cm^3 for specimen series D to 3.03 g/cm^3 for specimen series A, according to different mineralogical composition. No densities were determined in the previous investigations, yet according to *Foged (2009)*, this is an expected range for the considered rock types. The determination of densities is not associated with great difficulty, and can be performed by either sampling from the field or from cored specimens.

Determined mean point load indices from samples retieved from the field are approximately of the size 2.5-3.0 MPa, as opposed to the mean point load indices previously obtained from the core from boring B9201, which assumed values of 4.2-4.3 MPa in average. The discrepancy between the two data sets are interpreted as being effects of excavation disturbance, since the blasting induce microcracks in the grain structure of the rock, effecting the mechanical properties negatively. The ratio of compressive strengths relative to point load indices ranged from 13.2-33, a range which is expected according to the *ISRM Suggested Method* on the subject, even though it states a mean ratio equal to 20-25. The mean ratio in present report is only 17.9 in comparison.

Compressive testing yielded ratios between unconfined compressive strengths and indirect tensile strengths of 10.6 to 16.9, which is higher than the proposed ratio of 8-12 by *Foged (2009)*, and can be explained by the fact that the ratio of Foged is based on Danish limestone data, and the found ratios in this report are obtained for hard metamorphic and igneous rock. The ratio between the static modulus and the compressive strength ranges from 78 to 245, and the ratio between the dynamic modulus and the compressive strength ranges from 265 to 1040. The ratio between the dynamic and static moduli ranges from 2.9 to 4.3. The ratios do all follow an general increasing trend when the values from each rock type are plotted against each other, where especially

the latter two are significant, since a correlation between dynamic and static properties can provide estimates of the actual strength and deformability of the considered rock by means of determining a dynamic modulus from density and p-wave velocity measurements.

No clear correlation between p-wave velocities and compressive strength is seen in the data from present report. The dynamic modulus do seem to qualitatively yield better correlations between the considered parameters, such as compressive strengths and static moduli. This can be due to the fact that dynamic modulus incorporates both the density and the p-wave velocity, making this parameter more nuanced than the p-wave velocity alone. A larger data basis of compressive strengths and static and dynamic moduli needs to be utilized if the correlations are to be sufficiently described.

Measurements of Schmidt hammer rebound are in the access/maintenance tunnel obscured by the presence of shotcrete droplets, which does not make them desirably amenable for basing interpretations on. The profile along the tunnel would have provided information about weathering degrees, which can be useful when interpreting the velocity profile from refraction seismic profiling. The Schmidt rebounds from the pressure tunnel site provided a derived compressive strength, which is very comparable with the actual from unconfined compressive testing.

The internal cohesion and the friction angles determined in present report range from 5.7-21.4 MPa and 52.7-62.2 degrees, respectively. The high values of internal cohesion and friction angle are expected for hard igneous and metamorphic rock, *Foged (2009)*. The results are for the specimen series D, E, and F obtained utilizing only 1 indirect tensile strength, making the calculations of envelopes very uncertain, due to rock inherently is inhomogeneous. Though were the envelope parameters based on 5 different methods, making the envelopes certain, based on the given failure data.

The conversion from point load index to indirect tensile strength only introduced a minor error in the envelope calculations.

The poorest specimen was determined to be specimen series F. This is the case for compressive strength, (synthetic) indirect tensile strength, point load index, p-wave velocity, dynamic and static Young's modulus, friction angle and internal cohesion. This is concluded to be caused by the rock type has a significant content of biotite mica, which implied a weakening of the grain structure, and thereby negatively effecting mechanical and dynamic properties.

It can be discussed if the non-parallel specimen ends produced a non-uniaxial stress state in the specimens during unconfined compression. The tiltable upper loading platen should though counteract this effect, according to the *ISRM Suggested Method* on the subject.

Intact p-wave velocities ranged from 4.28 to 6.24 km/s for all considered rock types. These comprise the upper bound for obtainable in situ velocities in corresponding rock masses of the same rock type. Intact p-wave velocities for specimen series F, sampled from the access/maintenance tunnel, were determined to be 2.64 to 4.66 km/s. The lower velocity is interpreted as being primarily effected by the blasting during excavation, and is therefore considered invalid. The higher velocity is the upper bound for the velocities obtained from refraction seismic investigations, from which RQD values are estimated. The intact p–wave velocity from specimens

sampled from the pressure tunnel site is determined to be 3.56 km/s, which is lower than determined velocities from the access/maintenance tunnel, due to what is interpreted as higher weathering degree, and thereby larger susceptibility for excavation or blast related disturbance.

The refraction seismic profile in the access/maintenance tunnel yielded an average velocity of 3.93 km/s, and ranged from 3.14-4.49 km/s. These velocities lie in the lower range of velocities obtained from the refraction seismic investigations of 1985, which ranged from 4.2-5.3 km/s for the more competent rock in the same area. The effects of excavation disturbance on the refraction seismic data are though supposedly minimized, since p-wave velocities are determined from first arrivals of waves propagating through the locally fastest path, which in turn represent the locally most competent rock, *Barton (2007)*.

The RQD values calculated as 100 times the square of the ratio between laboratory and field velocities, as proposed in *Barton (2007)*, are very comparable with the mapped values of RQD of Istak, which in turn also resembles trends in the mapped GSI. No fatal weakness zones are identified from the refraction seismic surveys. The average mapped value of the RQD along the access/maintenance tunnel is 80, compared with a calculated mean of 74. For the pressure tunnel site a calculated RQD value was 42, compared with the mapped value of 40. This is the fact in spite of the RQD being directionally dependent, which also is the case for the seismic profiling, which does not detect joints parallel to the profile. Further is the RQD mapped as the poorest occurrence on the mapped tunnel section, which might not coincide with the placement of the seismic profile. So the refraction seismic method does provide means of indirectly estimating the RQD, if combined with laboratory measurements as a reference. But it should be noted that the refractions seismic method cannot detect minor defect such as slickensided joint walls, which govern the mechanical stability of the considered rock. This substantiates why engineering geological mapping is to the performed as a supplement to refraction seismic investigations, since these will detect such discontinuities. The engineering geological mapping further provide means of constructing a failure envelope, when combined with laboratory testing for obtainment of strength parameters. This cannot be done satisfactory based on seismic data alone, but rough estimates of rock mass parameters can though be provided, especially for use in early planning stages of a project.

8 Recommendations

Regarding the use of the refraction seismic method, it is recommended to use multichannel geophones for acquisition of both p- and s-wave data. The interplay between the ratio of v_p to v_s, is in Barton (2007), described as a more sensitive indicator of jointing than p-wave data alone. The obtainment of both these velocities will further give better understanding of correlations between dynamic and static elastic parameters.

Further will the use of tomographic inversion on the obtained travel times produce a more nuanced interpretation of the velocity distribution in the considered bedrock. While the plus/minus inversion method only can interpret low velocity zones as vertical regions, the tomographic inversion can supposedly interpret dipping low velocity zones, such as fault breccia. It is recommended to analyze, using for example ReflexW (see www.sandmeier-geo.de/Reflex/reflexw.htm for more information), a planar 2-D scenario of bedrock with a dipping low-velocity over which overburden soil is present. The software can then generate synthetic travel times, which one in MicroSoft Excel then can add random noise to. The software can then perform a tomographic inversion on the travel times including noise, such that it can be analyzed if the tomographic inversion method can detect the dip of the low-velocity zone. If so, it would be of interest to perform a tomographic inversion on the original data from the refraction seismic surveys from 1985, to see if the weakness zones found in profiles of S8503 and S8506 actually intersect the tunnel, as guessed upon during the project. The knowledge of the dip and strike of this weakness zone could have prevented the tunnel collapse, since it is believed, that this weakness zone is responsible.

To supplement refraction seismics performed on the surface, down-hole or cross-hole seismics should be performed to give information about the rock quality versus depth. This is substantiated by the fact that the RQD is directionally dependent, and that down-hole and cross-hole seismics would yield qualitatively different data than the surface refraction.

It is further recommended that correlation between dynamic moduli and compressive strength or static moduli is investigated more thoroughly. This means also that the stress-strain curves should be determined for only specimen deformations, and not including deformations metal plates, as done in this project. Further should a larger specimen basis be considered to give greater data density, which minimize the effect of rock being inhomogeneous by nature relative to the amount of data.

The dispersive nature of sonic waves in hard rock should be investigated under laboratory conditions, by using different frequencies to determine to what extent the sonic velocity is frequency dependent.

Since the GSI is directly used in the Hoek-Brown failure criterion, it would be relevant to investigate p-wave velocities in GSI-mapped areas, such to find a possible correlation between p-wave velocity and GSI, like the case for the correlation between p-wave velocity and the RQD.

Regarding the calculation of friction angle and internal cohesion, it is recommended that triaxial testing is used to produce other stress states than the simple stress states related to unconfined compression and Brazilian tests. This would make the failure envelopes more nuanced, since a greater range of stresses are obtained.

Intentionally left blank

9 References

Andersen, M. A. (1995): '*Petroleum research in Noth Sea chalk*'. Amaco Norway Oil Company and Rogaland Research.

Barton, N. (2007): 'Rock Quality, Seismic Velocity, Attenuation and Anisotropy'. Taylor and Francis Group. ISBN10: 0-415-39441-4.

Brady, E.H.G., Brown, E.T. (2004): '*Rock Mechanics for Underground Mining*'. Third edition. Springer, P.O. Box 17, 3300 AA Dordrecht, The Netherlands. ISBN10: 1-4020-2116-X.

Brandt, Inooraq (2008): '*Geophysical Investigations of Permafrost Related Structural Failures on Roads in Thule, Greenland*'. M.Sc. thesis at the Technical University of Denmark.

Deere, D.U. et al. (1967): '*Design of surface and near-surface construction*'. *Failure and Breakage of Rock*, pp. 237–302. New York Society of Mining Engineers of AIME.

Dufour, J., Foltinek, D. S. (1996): '*The Plus-Minus Time Analysis Method and its Implementation*'. Crewes Research Report – Volume 8. pp. 13.1-13.34.

Foged, N. (2009): Personal communications during this project.

Foged, N. (1979): *'Ingeniørgeologiske Undersøgelser af Kvartære Marine Leraflejringer på Vestgrønland. English: Engineering Geological Investigations of Quaternary Marine Deposits in West Greenland*'. Ph.D.-thesis at the Technical University of Denmark (Danish: Licentiatafhandling ved det daværende Institut for Teksnisk Geologi, DTH nu BYG•DTU).

Henriksen, N. (2005): 'Grønlands *Geologiske Udvikling fra Urtid til Nutid'*. Denmarks and Greenlands Geological Survey (GEUS). ISBN: 87-7871-163-0. Book written in Danish.

Hoek, E. (1983): *'Strength of jointed rock masses'*. 23rd Rankine lecture, Géotechnique, Vol. 23, No. 3, 1983, pp. 187-223.

Hoek, E. et al. (2002): *'Hoek-Brown failure criterion – 2002 Edition'.*

Hoek, E. (2006): '*Practical Rock Engineering*'. University of Toronto and Evert Hoek Consulting Engineer Inc.

Humlum, O & Christiansen, H.H. (2000): "Atlas over Grønland", Royal Danish Geographical Society, 2000.

Hunt, R. E. (2007): *'Characteristics of Geologic Materials and Formations - A Field Guide for Geotechnical Engineers'*. CRC Press, Taylor and Francis Group. ISBN10: 1-4200-4276-9.

International Society for Rock Mechanics (ISRM) Suggested Methods for: '-Determining Sound Velocity'. '-Determining Point Load Strength (1985)'. '-The Quantitative Description of Discontinuities in Rock Masses (1978)'. '-Determination of the Schmidt Hammer Rebound Hardness: Revised Version (2009)'. '-Determining Tensile Strength of Rock Materials'. '-the Complete Stress-Strain Curve for Intact Rock in Uniaxial Compression'. '-Land Geophysics in Rock Engineering'.

Lankston, R. W. (not dated): '*High Resolution Refraction Data Acquisition and Interpretation*'. Geo-Compu-Graph Inc., P. 0. Box 1848, Fayetteville, AR 72702-1848.

Madland et al. (2002): *'Temperature effects in Brazilian, uniaxial and triaxial compressive tests with high porosity chalk*'.

Mavko, G., Mukerji, T., Dvorkin, J. (2003): '*The Rock Physics Handbook – Tools for Seismic Analysis in Porous Media*'. Cambridge University Press. ISBN: 0-521-54344-4.

Nazarian, S. & Stokoe, II. (1983): '*Use of Spectral Analysis of Surface Waves Method for Determination of Moduli and Thickness of Pavement Systems*'.

Palmström, A. (2005): '*Measurements of and correlations between block size and rock quality designation (RQD)*'. Tunnelling and Underground Space Technology 20 (2005), pp. 362–377.

Palmström, A., Blindheim, T., Broch, E., (2002):'*The Q-system – Possibilities and Limitations*'. Fjellsprengningsteknikk - Bergmekanikk - Geoteknikk 2002 (Publication from Norway). pp. 41.1-41.44.

Pariseau , W. G. (2007): *'Design Analysis in Rock Mechanics'*. Malcolm McKinnon Endowed Chair, Department of Mining Engineering, University of Utah, Salt Lake City, Utah, USA. Taylor and Francis Group. ISBN10: 0-203-96825-5. pp. 1-15, pp. 175-229, pp. 473-551.

Redpath, B. B. (1973): '*Seismic Refraction Explorations for Engineering Site Investigations*'. Distributed by the U.S. DEPARTMENT OF COMMERCE, National Technical Information Service, 5285 Port Royal Road, Springfield, Virginia 22161. Written at the Explosive Excavation Research Laboratory Livermore, California.

Reynold, J. M. (1997): 'An *introduction to Applied and Environmental Geophysics'*. Reynolds Geo-Sciences, Ldt., UK. John Wiley and son.

Technical Organisation of Greenland (Danish abbreviation: GTO) (1985): '*Forundersøgelser: Vandkraft 1985 – Anlægsteknik: Delrapport 2 – Tasersuaq: Sisimiut/Holsteinsborg*'. Report written in Danish.